RICE UNIVERSITY

# Kinetic Energy Oscillations in Annular Regions of an Ultracold Neutral Plasma

by

**Sampad Laha**

A Thesis Submitted
in Partial Fulfillment of the
Requirements for the Degree

**Master of Science**

Approved, Thesis Committee:

---

Thomas C. Killian, Chairman
Assistant Professor of Physics and
Astronomy

---

Barry F. Dunning
Sam and Helen Worden Professor of
Physics

---

Ian M. Duck
Professor of Physics and Astronomy

Houston, Texas

April, 2005

# ABSTRACT

## Kinetic Energy Oscillations in Annular Regions of an Ultracold Neutral Plasma

by

Sampad Laha

A study of ion oscillations in the annular regions of a strontium plasma is reported. An ultracold neutral plasma is formed by photoionizing the $^1P_1$ electrons using a pulsed dye laser, and absorption spectroscopy is done on the $^2S_{1/2} - ^2P_{1/2}$ transition of the $Sr^+$ ion. The kinetic energy of the ions is then calculated using Doppler broadening of the spectrum. The variation of temperature with time is fit to a theoretical model of kinetic energy oscillation. The result of the fitting is presented in this thesis. The importance of an annular analysis of the absorption spectrum is demonstrated and the mathematical procedures employed to calculate the kinetic energy are developed. The oscillations are observed to be damped which is a characteristic of strongly coupled plasmas.

# Acknowledgments

I would like to dedicate my thesis to my family, whose upbringing and support has helped me reach this stage of my life and to Anushree, whose constant support and encouragement has always pushed me to keep going despite difficulties. I especially acknowledge the help and guidance given by my advisor, Dr. Thomas C. Killian. This thesis would not have been complete without his patience in explaining things so lucidly. I also acknowledge the help given out to me by all my labmates. Their presence makes working in the lab fun and rewarding. I also thank Dr. Ying-Cheng Chen, as a lot of this work was done with him. Finally, I would like to thank all the friends who have helped me directly or indirectly. It is because of people like them that this earth is such a nice place.

# Contents

# List of Figures

# Chapter 1
# Imaging ultracold plasmas

The materials that we are accustomed to on this planet usually come in three states of matter - solid, liquid or gas. But if we include the whole universe, then we will observe that nature (including our own Sun) exists more widely in a different state of matter - the plasma. In a plasma the thermal energy is usually so great that the electrons are liberated from the bonds of the nucleus, and they are now a separate entity too. The reason that plasma has been designated the fourth state of matter is because we may think of the collection of the positive and the negative entities to exist as gas, but the waves that exist in a plasma have much in common with the waves in a conducting solid, whereas the transport properties of a plasma are best described by equations developed for fluids.

## 1.1 Categories of plasma

Although there are different parameters that characterize plasmas, they can be very broadly classified into two categories - strongly and weakly coupled plasma. For a strongly coupled plasma, the ratio of the Coulomb potential energy to the kinetic energy, called the coulomb coupling parameter or $\Gamma$, is greater than 1. Whereas, for weakly coupled plasma, the coulomb coupling parameter, $\Gamma$, is less than 1. A schematic diagram of different types of plasmas that can exist is shown in Fig. 1.1

where their temperatures and densities are compared. In most cases, high (thermal) energy is needed to liberate the electrons from the nucleus and this gives the electron lots of kinetic energy, and thus a weakly coupled plasma results. But in some stages of collapsed stars, like white dwarfs and neutron stars, the interparticle distances are so small that plasma naturally exists in a strongly coupled state. There is also another way of attaining a strongly coupled plasma - by reducing the temperature of both the positive and negative constituents of the plasma. It is here that the field of ultracold plasmas comes in.

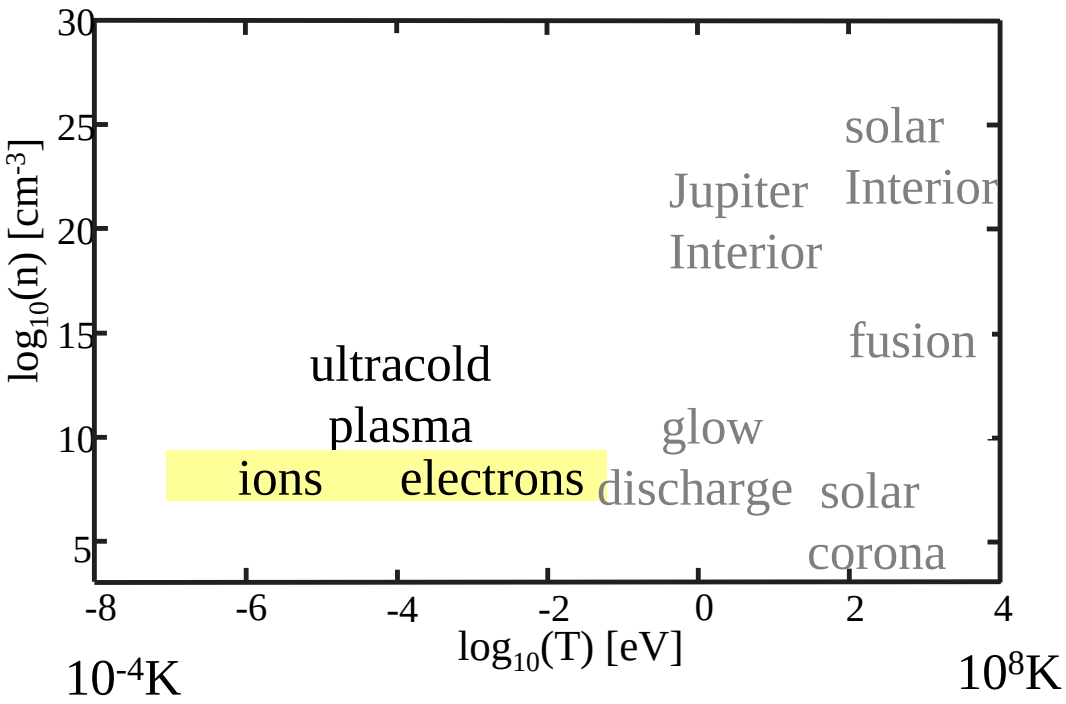


**Figure 1.1** Some types of plasma that can exist

## 1.2 Introduction to ultracold neutral plasma

Creating ultracold neutral plasmas in the laboratory environment was first reported [1] in National Institute of Standards and Technology, Gaithersburg, Maryland. The plasma was produced by photoionizing laser cooled xenon atoms. The temperature of electrons in this type of plasma can vary between 1-1000 K (depending mostly on the frequency of the photoionizing laser) and the ion temperature is around 1K. The charge carrier density can be as high as $10^{16}$ m$^{-3}$.

In our laboratory, to produce plasma, strontium atoms are first laser cooled. The atoms are cooled in a magneto-optical trap [2] on the $^1S_0 - ^1P_1$ dipole allowed transition at 461 nm. The neutral atoms have a temperature of about 20 mK with peak density of about $(4 \pm 2) \times 10^{10}$ cm$^{-3}$ and total number of atoms of about $(6 \pm 1) \times 10^8$ [3]. After turning the MOT magnets off, the atoms that are in the $^1P_1$ excited state are photoionized with a 10 ns pulsed dye laser [4]. The wavelength of the dye laser is tuned to just above the ionization continuum. Because of the small electron-to-ion mass ratio, nearly all the energy of the photon is transferred to the electron's kinetic energy ($E_e$). $E_e/k_B$ can be as low as 100 mK which is the bandwidth of the laser. A schematic of the MOT and the photoionization is shown in Fig. 1.2.

The charge distribution and dynamics of the plasma can be probed by employing charged particle detection techniques. Information about the behavior of the plasma

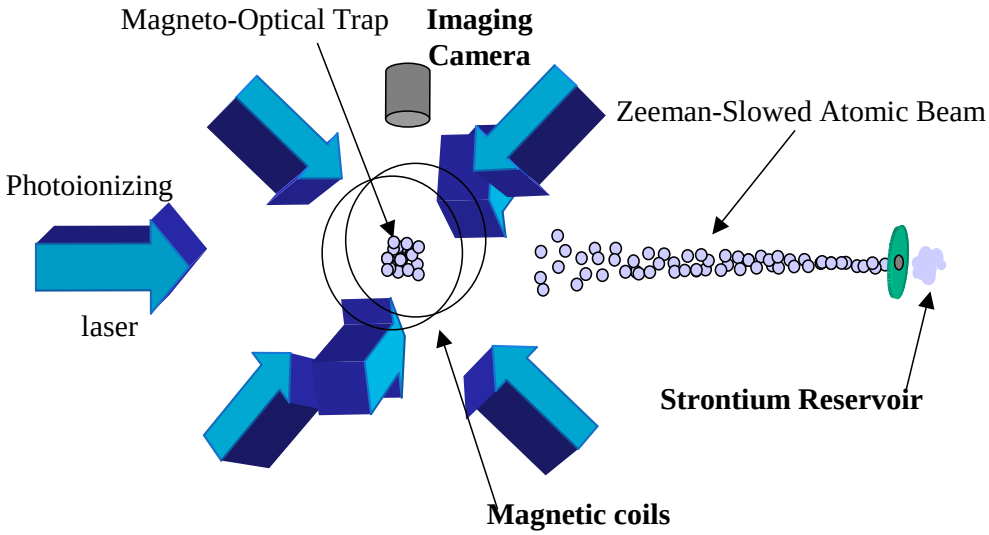


**Figure 1.2** Basic experimental setup of the MOT and photoionization

can be obtained with this simple technique. In this technique, a variable electric field is applied to attract the charged particles (electrons or ions). The detection signal is observed with respect to time and it can be related to the magnitude of the electric field. This gives us very crucial information about the way the plasma evolves with time.

In our lab, we also use a charged particle detection system to probe the plasma. A description of our detection system is given in Appendix C. The main drawback in the charged particle detection technique is that it destroys the plasma. A non-destructive way of probing the plasma is by absorption imaging the plasma. This method is described in the following section.

## 1.3 Imaging ultracold plasmas

One of the advantages of absorption spectroscopy to probe the plasma is that it is a non-destructive and *in situ* method. The charged particle detection technique can give information only about the average density of the plasma, whereas by absorption spectroscopy the plasma can be resolved both spatially and temporally. The ions cast a shadow when illuminated by a laser of proper wavelength and the image recorded on a charged coupled device (CCD) camera and this image is analyzed. Strontium ions ($Sr^+$) have a transition, $^2S_{1/2} - ^2P_{1/2}$, at wavelength 422nm. In the experiments, light of 844 nm is frequency doubled to 422 nm and the absorption spectroscopy is done [3, 5].

In principle, absorption spectroscopy is simple. The absorption coefficient is first related to the laser intensity when the absorbent is present and when it is not. Following Beer's law, the optical depth of the image is

$$OD(x, y) = ln \left[ \frac{I_{background}}{I_{plasma}} \right], \tag{1.1}$$

where $I_{plasma}$ and $I_{background}$, as in Fig. 1.3, are the intensity of the laser when the plasma is present and when it is not. The optical depth is found out directly from the experimental image of the plasma. And then, as shown in chapter 3, the OD is related to the underlying physical parameters of the plasma, more specifically, the effective temperature.

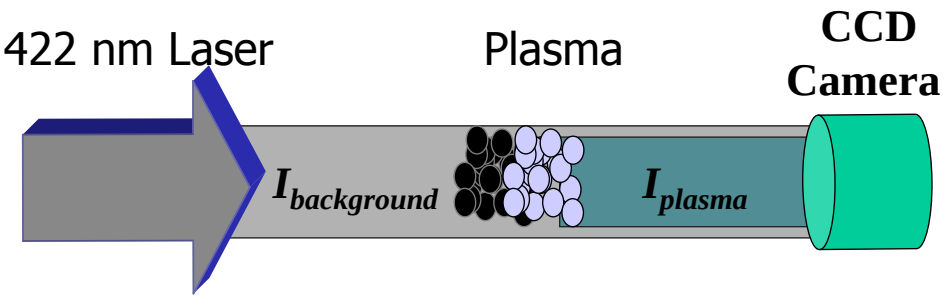


**Figure 1.3** Absorption imaging of Sr plasma. The 422 nm light casts a shadow of the Sr ions, which have a resonant transition at 422 nm. The image is recorded on an image intensified charge-coupled device (CCD) camera.

# Chapter 2
# Ion dynamics in a plasma

## 2.1 Introduction

In a plasma, coulombic interactions result in many phenomena. Ion oscillation and expansion of the plasma are two examples. In this chapter, the origins of ion and electron oscillations in a plasma are explained. The effect of variation of the density on the oscillation is also shown, which results in the need to do annular analysis. Finally, there is a short introduction to the expansion of a plasma.

## 2.2 Plasma oscillations in constant density

Plasma by definition is a collection of charged particles that are free to move by external influence. If the equilibrium condition is changed inside a plasma, the particles will try to reach equilibrium again, and this is what gives rise to any kind of oscillation. If we consider electrons in the plasma, then it is easy to show that a displacement of the electrons from the ions results into a restoring simple harmonic force, and the electrons undergo oscillations whose frequency is given by $\omega_{pe} = \sqrt{n_{0e}e^2/m_e\epsilon_0}$. This quantity is called the electron plasma frequency, and is the resonant frequency of oscillation at which the electrons in a plasma would oscillate.

The situation is different in the case of ion motion. Ion-plasma oscillations are observed only when the wave vector, $k > 1/\lambda_D$, where, $\lambda_D = \frac{1}{\omega_{pe}}\sqrt{k_B T_e/m_e}$ is the

electron Debye screening length with $T_e$ being the electron temperature. This means that the electrons are not effective in screening out the coulombic force between the ions. The ion plasma frequency in this case has a value of $\omega_{pi} = \sqrt{n_{0i}e^2/m_i\epsilon_0}$, which is similar to that of the electronic plasma frequency. However, when $k < 1/\lambda_D$, the frequency increases linearly with $k$ and is given by $\omega = C_s k$. This is called the ion acoustic wave because as we will see below, the expression for the phase velocity, $C_s = \sqrt{k_B T_e/m_i}$, is independent of $k$.

The above argument can be understood from the dispersion relationship of ion acoustic waves in a two component plasma, given by [7]

$$1 - \frac{\omega_{pe}^2}{\omega^2 - k^2 v_e^2} - \frac{\omega_{pi}^2}{\omega^2 - k^2 v_i^2} = 0, \tag{2.1}$$

where, $k = 2\pi/\lambda$ is the wave vector and $v_{e,i} \simeq \sqrt{k_B T_{e,i}/m_{e,i}}$ are the electron and ion thermal velocities. Assuming that $\omega \ll \omega_{pe}$ and $T_e \gg T_i$, which results in the approximation $v_i \ll \omega/k \ll v_e$, the dispersion relation becomes,

$$1 + \frac{\omega_{pe}^2}{k^2 v_e^2} - \frac{\omega_{pi}^2}{\omega^2} = 0 \tag{2.2}$$

$$\Rightarrow\ 1 + \frac{1}{k^2\lambda_D^2} - \frac{\omega_{pi}^2}{\omega^2} = 0 \tag{2.3}$$

$$\Rightarrow\ \omega = \frac{kC_s}{\sqrt{1 + k^2\lambda_D^2}}. \tag{2.4}$$

It is clear that when $k \to 0$, we get $\omega = C_s k$, establishing the ion acoustic wave phenomenon. It is worth mentioning that the phase velocity, $C_s$, is driven by the electronic energy ($T_e$) but the inertia is provided by the mass of the ions ($m_i$).

At large k values however, the frequency of the wave approaches the ion plasma frequency, $\omega_{pi}$. This is because $k = 2\pi/\lambda \simeq 2\pi/\lambda_D$, and as k becomes large, the effective screening by the electrons decreases. This decouples the electrons and the ions, and in this case the frequency of the ion acoustic wave approaches $\omega_{pi}$. The ion acoustic branch and the ion oscillation branch can be seen clearly in Fig. 2.1.

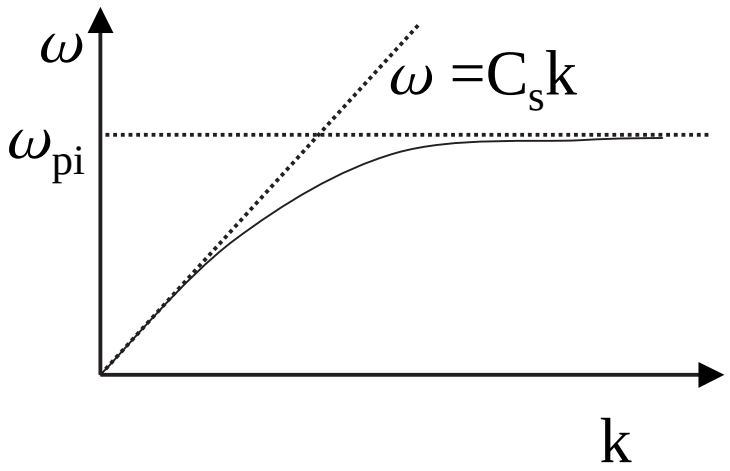


**Figure 2.1** Dispersion in ion acoustic wave for a two component ion-electron plasma. At low k, the phase velocity approaches a constant $C_s$, also called the ion acoustic wave velocity. And at high k values, the frequency approaches the ion plasma frequency, $\omega_{pi}$

.

Ion plasma oscillations are central to the thesis, so let us get a more intuitive picture of those. Physically, ion plasma oscillations can be visualized by considering ions in a body centered cubic (BCC) lattice configuration, where the body centered ion oscillates under the electrostatic attraction of the other ions at the vertices. The theory followed here is similar to that of a simple harmonic motion, where the change in potential energy from the mean position varies quadratically with the displacement

($U \sim \frac{1}{2}kx^2$) and the frequency of oscillation is given by $\sqrt{k/m}$. It should be noted however that the inter-ionic spacing in the example considered has to be lower than the electron Debye screening length, so that the ion electrostatic forces are not shielded out by the fast moving electrons. A unit cell of the lattice is shown in the Fig. 2.2, where the length of the cube is taken to be equal to 2a to simplify our calculations.

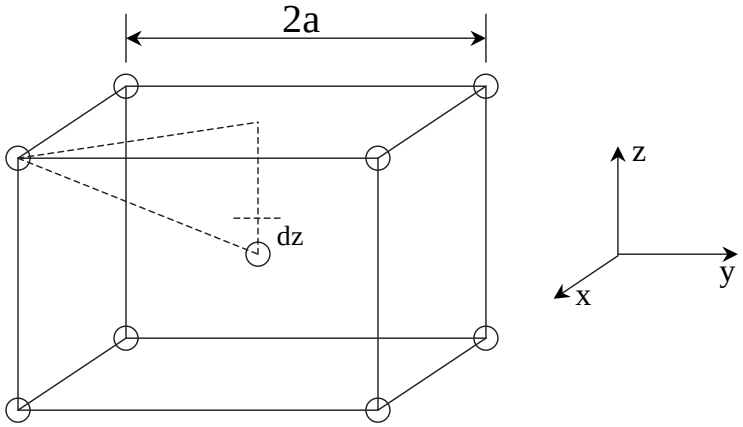


**Figure 2.2** Ions in a BCC lattice. The body centered ion is displaced by a distance dz, and a restoring force develops which makes the ion oscillate about its mean position.

Considering only the nearest neighbors, the total potential energy of the body centered ion in its mean position is given by

$$U = \frac{8}{4\pi\epsilon_0}\frac{e^2}{\sqrt{3}a}. \tag{2.5}$$

Now, considering that the central ion has been displaced by a distance $dz$ along the positive z-axis, its distance from the top four ions in first order of dz will be equal to $\sqrt{3a^2 - 2adz} \simeq \sqrt{3}a(1 - dz/3a)$. Similarly, the distance of the central ion from the bottom four ions will be equal to $\sqrt{3}a(1 + dz/3a)$. Thus, the new potential energy of

the central ion is equal to

$$U' = \frac{4}{4\pi\epsilon_0}\frac{e^2}{\sqrt{3}a}\left(\frac{1}{1-\frac{dz}{3a}}+\frac{1}{1+\frac{dz}{3a}}\right) \quad (2.6)$$

$$= \frac{4}{4\pi\epsilon_0}\frac{e^2}{\sqrt{3}a}\left(\frac{2}{1-\left(\frac{dz}{3a}\right)^2}\right) \quad (2.7)$$

$$\simeq \frac{8}{4\pi\epsilon_0}\frac{e^2}{\sqrt{3}a}\left(1+\left(\frac{dz}{3a}\right)^2\right). \quad (2.8)$$

The density of the ionic lattice, $n_{0i}$ (taking the packing fraction of BCC to be 0.68) is given by

$$\Rightarrow \qquad \frac{1}{n_{0i}} = \frac{1}{0.68}\times\frac{4}{3}\pi\left(\frac{\sqrt{3}a}{2}\right)^3 = \frac{1.47\times 4\pi\sqrt{3}a^3}{8}. \quad (2.9)$$

So the change in potential energy is given by $\Delta U = U' - U = (e^2 n_{0i}/6.12\epsilon_0)dz^2$ which is a quadratic in dz. The frequency of the harmonic oscillation is thus given by $\sqrt{e^2 n_{0i}/3.06 m_i \epsilon_0} = 0.6\omega_{pi}$, which is very close to the ion plasma frequency $\omega_{pi}$, considering that we only took the effect of nearest neighbors into account in our calculations.

Now that the origin of plasma oscillation is established, it is easy to see that the kinetic energy of the particles will oscillate with twice the ion-plasma frequency. It is like any other oscillation where the potential energy is converted to kinetic energy and vice versa. A schematic of this motion is shown in Fig. 2.3.

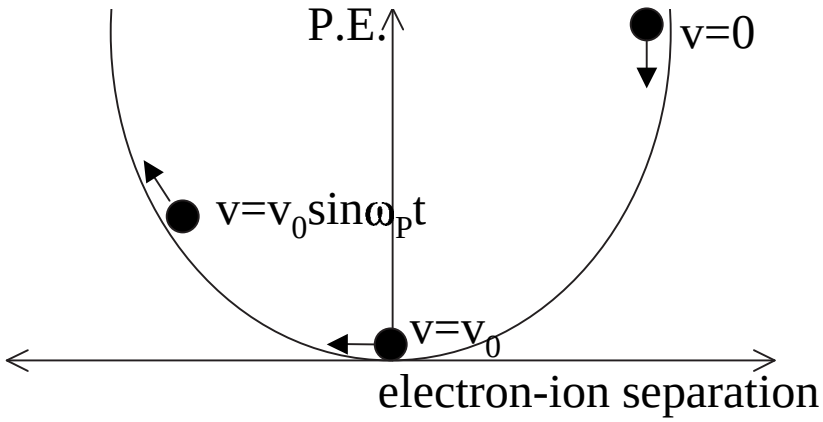


**Figure 2.3** Ion Oscillation in plasma. The figure shows the variation of ion kinetic energy in a simple harmonic potential. The frequency of the oscillation is the ion plasma frequency

## 2.3 Expression of temperature considering ion oscillation

Rigorously, we can only relate the kinetic energy to the temperature when local thermal equilibrium is established. The plasma in our case reaches local thermal equilibrium in a timescale of $\sim \pi/\omega_{Pi}$. We can assign an effective temperature of the ions, $T_{eff}$, which describes the average kinetic energy of the ions $\left(\frac{3}{2}k_B T_{eff} = \frac{1}{2}m\left\langle v^2\right\rangle\right)$. A simple expression for this effective ion temperature of ion considering the ion oscillations can be derived as follows. If we assume the velocity of the ion to vary as $v_0 sin\omega_{Pi}t$, where, $\omega_{Pi} = \sqrt{n_{0i}e^2/m_i\epsilon_0}$ is the ion plasma frequency, then from simple kinetic theory we know that temperature, $T_{eff} \propto v^2$. Thus, the effective temperature of the ions can be written as

$$T_{eff}(t) \propto sin^2(\omega_{Pi}t) \tag{2.10}$$

$$\Rightarrow \quad T_{eff}(t) \equiv T_i\,[1 - cos(2\omega_{Pi}t)]. \tag{2.11}$$

In reality, the ionic motion may not be free, and we incorporate this by including a damping term in the temperature expression. Taking the effect of this damping, the ionic temperature is written as

$$T_{eff}(t) = T_i\ [1 - cos(2\omega_{Pi}t)e^{-\alpha\omega_{Pi}t}], \tag{2.12}$$

where we have assumed a certain form of the damping and will discuss this later. In the expression, $\alpha$ is a measure of the damping and when no damping is present $\alpha = 0$. It is clear from the above equation, that at long time intervals, the oscillations die out due to the damping in the plasma. Thus $T_i$ is the locally equilibrated temperature of the ion. Its calculation is shown in sub-section 2.3.1.

### 2.3.1 Calculating the locally equilibrated temperature

Ions in a plasma have relatively low kinetic energy immediately after formation (photoionization). Their spatial position is highly uncorrelated and this has a higher Coulombic potential energy compared to that of a regular lattice structure [8]. Therefore, as the ions equilibrate to their lower potential energy configuration, the potential energy is converted to kinetic energy. This phenomenon is called disorder induced heating [9].

It is shown in [9] that if the ionic gas is initially highly uncorrelated and the ions interact through the screened Coulomb interaction, $u_Y(r) = e^2\mathrm{exp}(-\mathrm{r}/\lambda_\mathrm{D})/\mathrm{r}$, with $\lambda_D = \sqrt{\epsilon_0 k_B T_e/n_e e^2}$ the electron Debye screening length, then the equilibrium

temperature is given as

$$T_i = \frac{2}{3}\frac{e^2}{4\pi\epsilon_0 a k_B}\left|\tilde{U}(n_i,\Gamma_i) + \frac{\kappa(n_i,T_e)}{2}\right|. \tag{2.13}$$

Here, $\kappa = a/\lambda_D$, $\tilde{U} \equiv \frac{U}{N_i e^2/4\pi\epsilon_0 a}$ is the excess potential energy per unit particle in units of $e^2/4\pi\epsilon_0 a$ and $\Gamma_i = e^2/4\pi\epsilon_0 a k_B T_i$ is the coulomb coupling parameter for the ions. The quantity $\tilde{U}$ as a function of $\Gamma$ and $\kappa$ is tabulated in [10]. As can be seen from the above equation, the excess energy, $\tilde{U}$ is a function of $\Gamma_i$ and hence of $T_i$. For a given peak density, $n_0$, and electron temperature, $T_e$, we can solve the above equation by iterative method and obtain a distribution of the ionic temperature $T_i$. The Matlab code used to calculate this temperature is given in Appendix A.

## 2.4 Dephasing of oscillation - Need to do annular analysis

In the above section, the oscillations were considered when the ionic density is constant and not varying with position. But in reality, the ions have a Gaussian density distribution with respect to position. They will not have a constant plasma frequency or $T_i$, but these will vary with density. This presence of many intrinsic plasma frequencies in the medium, slowly takes the oscillations out of phase with each other, and this results in what is called dephasing, where the oscillations appear to die out sooner than they should. As shown in Fig. 2.4, all oscillations start out with the same phase, but eventually they fall out of phase even if $\alpha = 0$ (Eqn. 2.12). The result is a sine wave whose amplitude decreases progressively with time.

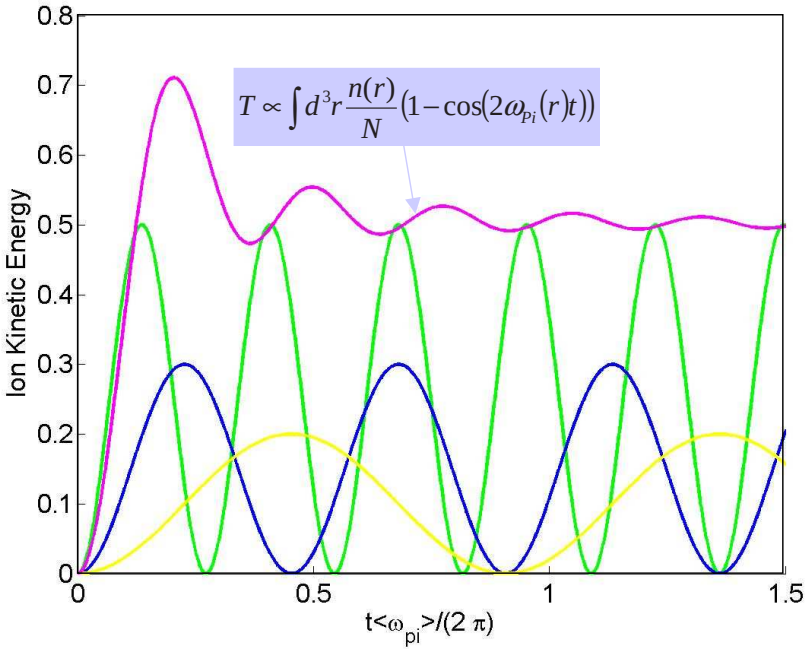


**Figure 2.4** Dephasing of oscillations in plasma. Even when oscillations start out with the same phase, they fall out of phase after certain time. The resultant is an oscillation whose amplitude decreases progressively with time.

It is due to this variation of density and ion-plasma frequency that the need to probe the density as a function of position arises. To do this, we divide the analysis of the plasma into concentric cylinders around the laser beam - each having the same number of ions and less density variation than the entire cloud. This results into annular cross sections in a two dimensional image of the plasma. In the image of the whole plasma, the oscillations die out soon because of dephasing. But, in the annular regions, plasma oscillations should be more prominent and easier to analyze. The effects of dephasing should be clear if we compare the oscillations in the whole plasma to that in the annular regions and we can determine if other damping processes

are important. This proves that the position-variance of the density indeed has an effect on the oscillations. In order to incorporate the change in density, the expression for the average effective temperature in this case is thus written as

$$T_{eff}(t) = \int_{\rho_1}^{\rho_2} d\rho \int_{-\infty}^{\infty} dz \ (2\pi\rho)\frac{n_i(r)}{N} T_i(r)[1 - cos(2\omega_{Pi}(r)t)e^{-\alpha\omega_{Pi}(r)t}], \tag{2.14}$$

where, we have used cylindrical coordinates with $\rho_1$ and $\rho_2$ indicating the cylindrical boundary of the annular regions and $r^2 = \rho^2 + z^2$. Here, notice that the locally equilibrated temperature, $T_i(r)$ is a function of position because in Eqn. 2.13 the density is a function of position.

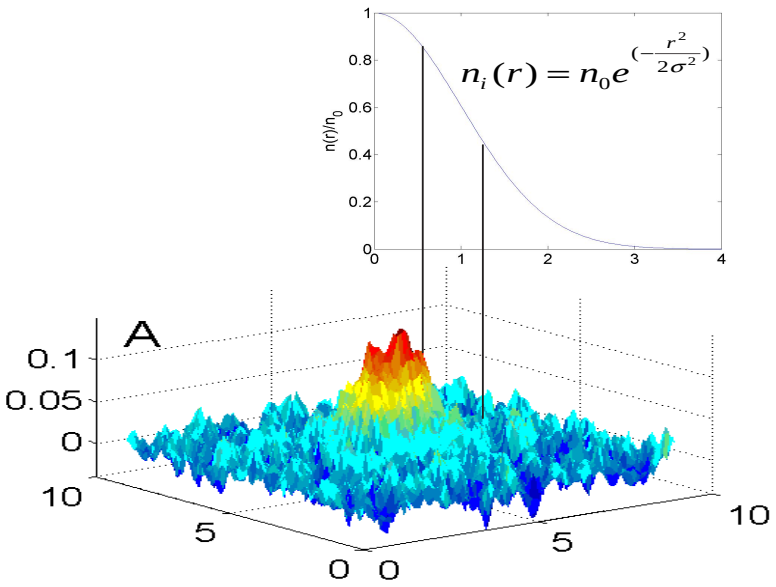


**Figure 2.5** Analyzing annular regions of plasma. Since the density is a function of the radial distance, if we can analyze a small annular section of our plasma image we can better probe the density variation of the plasma. This also reduces the dephasing effects in the plasma oscillations.

To define the annular regions, we divide the image of the plasma into three re-

gions, each having the same number of ions. These annular regions have cylindrical symmetry with the axis aligned with the direction of the laser propagation. The density of the plasma in our case peaks at the center (r=0) and then falls off roughly satisfying a Gaussian expression. The density distribution is written as

$$n_i(r) = n_0 \exp\left(\frac{-\mathrm{r}^2}{2\sigma^2}\right), \tag{2.15}$$

where $n_0$ is the peak density and $\sigma$ is a measure of size of the cloud. To find the limits, we denote the boundary of the annular regions by $\rho_1$ and $\rho_2$. The total number in each annular sections is thus given by

$$\int_{\rho_1}^{\rho_2} d\rho \int_{-\infty}^{\infty} dz \; (2\pi\rho) n_i(\rho, z) = \frac{1}{3} N_i, \tag{2.16}$$

where, $N_i$ is the total number of ions. The above equation can be solved for three coaxial regions, centered at $\rho = 0$. The three regions thus obtained are given by $(\rho_1, \rho_2) = (0, 0.9),\ (0.9, 1.48),$ and $(1.48, \infty)$ in units of $\sigma$. For the remainder of this thesis, these will be referred to as region 1, region 2 and region 3 respectively. The whole volume of the plasma will be referred to as region 0.

## 2.5 Expansion of plasma

In this section, I briefly describe another phenomenon which results in temporal change in temperature of the plasma. The electrons are held in the coulomb space charge of ions [1] but pressure of the electron gas accelerates the ions radially and eventually causes them to expand. [11, 12].

The expansion of a plasma is characterized by the expansion time given by

$$t_{exp} = \frac{\sigma_i}{T_e}\sqrt{\frac{m_i T_{i,ave}}{k_B}}, \tag{2.17}$$

where, $T_e$ is the electron temperature and $T_{i,ave}$ is the average temperature of the ions. This expansion time ($t_{exp}$) is the time at which the ion expansion velocity becomes comparable to the thermal velocity. The expansion will be rapid when the electrons have high kinetic energy (large $T_e$) and the expansion will be slow when the electrons have low kinetic energy (small $T_e$). This fact is clearly demonstrated in our data too and is shown in the chapter on data analysis (Fig. 4.3 and Fig. 4.4).

Although, the thesis is mainly focused on ion-plasma oscillations, the phenomenon of expansion will be incorporated to extract the effective temperature of the ions from the Doppler broadened spectrum. This process is explained in detail in the next chapter.

# Chapter 3

# Determining the ionic temperature

## 3.1 Introduction

Behind every experiment there is an underlying goal to extract a physical parameter from the results. In our case, the effective temperature is the most powerful parameter. It can be extracted by analyzing the absorption spectrum. By knowing the temperature and its variation with respect to position and time, many useful conclusions can be made, such as the existence of local thermal equilibrium of the plasma and kinetic-energy oscillations of the plasma.

This chapter is a short guide to the procedures employed to find the effective temperature of the ions. In the beginning section, calculation of the effective temperature for the whole volume of the plasma is described. Although the main focus of the thesis is on annular regions of the plasma, the analysis for the whole volume makes the procedure easy to understand and a better physical picture can be grasped. After this, the effects of electronic screening on the ion temperature is discussed, and then the temperature extraction for the annular cases will be described. The analysis for the whole volume closely follows [13] but the annular analysis is completely new.

## 3.2 Extracting the temperature of ions from the image.

When we study the variation of intensity of light with respect to frequency, the result is known as the spectrum. If a laser beam passes through a substance, then the spectrum obtained after passage contains information about the substance. Ideally, there should be sharp peaks or dips in the spectrum. Because of other effects, like collisions, non-zero thermal velocity, electric or magnetic fields, the spectrum is usually spread about the peak positions. This spread gives us information about the magnitude of the effects. For example, the temperature of the ions is directly related to their kinetic energy and velocity and hence to the Doppler broadening of the spectrum they produce. In reality, the Doppler broadening of the spectrum is used to calculate the temperature of the ions. We fit the spectrum to a Voigt profile (which is a convolution of Doppler and natural broadening), and obtain the effective temperature from the fit. A typical Voigt fit to the absorption spectra of our plasma is shown in Fig. 3.1, where the increase in the linewidth with the delay time is very clear.

In absorption spectroscopy, the optical depth (OD) gives us a measure of how much laser light has been absorbed. For the laser beam propagating along the positive z-axis, the OD is written as

$$OD(x,y) = \int_{-\infty}^{\infty} n_i(\vec{r})\alpha\Big(\nu, T_i(\vec{r})\Big)dz, \tag{3.1}$$

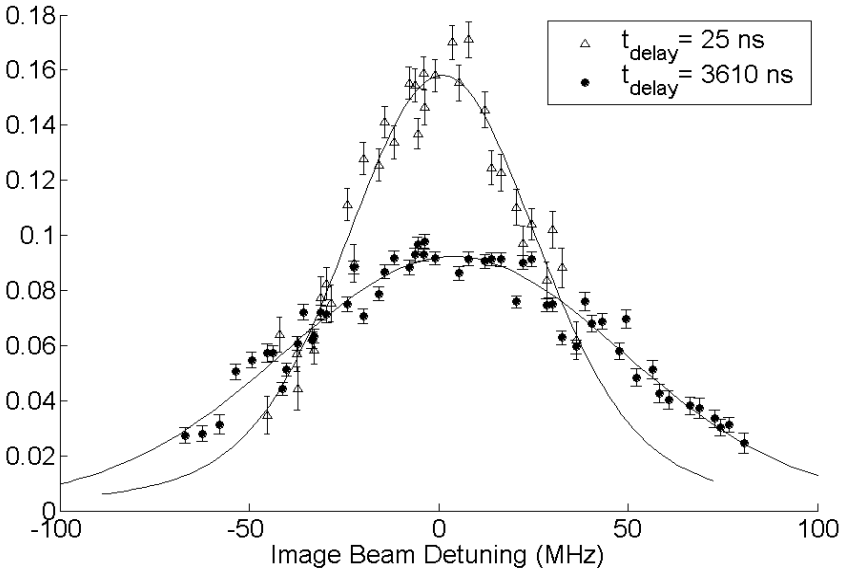


**Figure 3.1** Voigt fitting of the absorption spectrum with respect to the detuning. The y-axis is the average of the absorption cross-section.[3]

where, $n_i(\vec{r})$ is the density of the ions, $\alpha\Big(\nu, T_i(\vec{r})\Big)$ is the absorption cross section of the ions at the frequency $\nu$. The dependence of $\alpha$ on the temperature helps relate the OD to the temperature of ions. It should also be pointed out that the equilibration temperature of the ions is related to density, and as the density varies with position, so does the temperature. We can sum the OD over the image surface and get the absorption spectrum $S(\nu)$, which is given by

$$S(\nu) \equiv \iint OD(x,y)dxdy = \int_V n_i(\vec{r})\alpha\Big(\nu, T_i(\vec{r})\Big)d^3r. \tag{3.2}$$

In order to extract physical meaning from the above equation, we relate the absorption cross section to underlying physical parameters, like the temperature of the ions and the resonance frequency of the ionic transition. Through the atomic gain co-

efficient, the absorption cross section is related [14] to the complex part of the atomic susceptibility, $\chi_c(\nu)$, as

$$\begin{aligned} \alpha(\nu) &= \frac{2\pi}{\Delta N \lambda}\chi_c(\nu) \\ &= \frac{3^*\lambda^2}{2\pi}\frac{\gamma_0}{\gamma_{eff}} \times \frac{1}{1+\left[\frac{2(\nu-\nu_0)}{\gamma_{eff}/2\pi}\right]^2}, \end{aligned} \tag{3.3}$$

where $\Delta N$ is the population difference between the ground and the excited states, $\nu_0$ is the resonance frequency of transition and $\gamma_{eff}$ is the full-width half-maximum (FWHM) of the observed transition. If the dominant broadening is because of laser linewidth and natural linewidth, then, $\gamma_{eff} = \gamma_0 + \gamma_{laser} =$, where, $\gamma_0 = 2\pi \times 22 \times 10^6$ rad/s is the natural linewidth and $\gamma_{laser} = 2\pi \times (5 \pm 2) \times 10^6$ rad/s is the laser linewidth. The factor $3^*$ in the above expression can have values between 0 and 3, but due to the random alignment of the ions, in our case, $3^* = 1$ [14]. *

In the expression for $\alpha$ in Eqn. 3.3, we do not take into account the Doppler broadening of the linewidth due to the non-zero temperature of the ions. The broadening processes are statistically independent and each infinitesimal frequency band of the Lorentzian may be considered to be Doppler broadened. The resultant absorption coefficient is thus written as the convolution of both the contributions, which is

*The analysis shown here is taken from [13]. The RHS of Eqn. (7) in [13] needs to be multiplied by a factor of $\frac{\gamma_0}{\gamma_{eff}}$

commonly called the Voigt profile.

$$\alpha(\nu, T_i) = \frac{3^*\lambda^2}{2\pi}\frac{\gamma_0}{\gamma_{eff}}\int_{-\infty}^{\infty} ds \frac{1}{1+\left[\frac{2(\nu-s)}{\gamma_{eff}/2\pi}\right]^2}\frac{1}{\sqrt{2\pi}\sigma_D[T_i(r)]}\exp\left[-\frac{(\mathrm{s}-\nu_0)^2}{2\sigma_{\mathrm{D}}^2[\mathrm{T_i(r)}]}\right], \quad (3.4)$$

where, $\sigma_D(T_i) = \frac{1}{\lambda}\sqrt{\frac{k_B T_i}{m_i}}$ is the Doppler width. The factor $1/\sqrt{2\pi}\sigma_D[T_i(r)]$ in the integral takes care of the fact that $\int \alpha(\nu)d\nu = \int \alpha(\nu, T_i)d\nu$.

Combining equations 3.4 and 3.2, we get the expression for the absorption spectrum as

$$\begin{aligned} S(\nu) &= \frac{3^*\lambda^2}{2\pi}\frac{\gamma_0}{\gamma_{eff}}\int_{-\infty}^{\infty} ds \frac{1}{1+\left[\frac{2(\nu-s)}{\gamma_{eff}/2\pi}\right]^2} \times \\ &\qquad \int_V d^3r n_i(\vec{r})\frac{1}{\sqrt{2\pi}\sigma_D[T_i(r)]}\exp\left[-\frac{(\mathrm{s}-\nu_0)^2}{2\sigma_{\mathrm{D}}^2[\mathrm{T_i(r)}]}\right]. \quad (3.5) \end{aligned}$$

The spatial integration in equation 3.5 can be simplified by assuming an expression for $T_i(r)$. It is shown in [15] that if we neglect electronic screening (which is true for high $T_e$), the expression for temperature can be approximated by

$$\begin{aligned} T_i(r) &= C'\frac{e^2}{4\pi\epsilon_0 a(r) k_B} = C'\sqrt[3]{\frac{4\pi}{3}}\frac{e^2}{4\pi\epsilon_0 k_B} \times [n_i(r)]^{1/3} \quad (3.6) \\ &= T_{i,max}e^{-r^2/6\sigma^2}, \quad (3.7) \end{aligned}$$

where, $a(r) = (4\pi n_i(r)/3)^{-1/3}$ is the spacing between the neighboring ions, $T_{i,max}$ is the temperature of the ions at r=0 and a Gaussian distribution of the density is assumed $n_i(r) = e^{-r^2/2\sigma^2}$. It should also be pointed out that the temperature in

equation 3.7 is the locally equilibrated temperature of the ions, which the ions can reach in a time scale of the order of the inverse plasma frequency, $(\pi/\omega_{pi})$, which is typically equal to 100 ns. The plasma temperature reaches global thermal equilibrium in a time scale of the order of $\sigma/v$, where, $\sigma$ is a measure of the size and $v$ is the ion acoustic wave velocity. Usually, this time is of the order of 1-2 $\mu$s, although in our lab this timescale has not been explored and global thermalization has not yet been observed.

Putting the expression of temperature from equation 3.7 into 3.5, the expression for the spectrum modifies to

$$\begin{aligned} S(\nu) &= \frac{3^*\lambda^2}{2\pi}\frac{\gamma_0}{\gamma_{eff}}\int_{-\infty}^{\infty} ds \frac{1}{1+\left[\frac{2(\nu-s)}{\gamma_{eff}/2\pi}\right]^2} \times \\ &\qquad \int d^3r n_{oi} \frac{e^{-r^2/2\sigma^2} e^{r^2/12\sigma^2}}{\sqrt{2\pi}\sigma_{D,max}} \exp\left[-\mathrm{e}^{\mathrm{r}^2/6\sigma^2}\frac{(\mathrm{s}-\nu_0)^2}{2\sigma^2_{\mathrm{D,max}}}\right], \end{aligned} \quad (3.8)$$

where, $\sigma_{D,max} = \frac{1}{\lambda}\sqrt{\frac{k_B T_{i,max}}{m_i}}$ is the Doppler width corresponding to the maximum temperature, $T_{i,max} = T_i(r=0)$. As shown in Fig. 3.2, the spatial integration in the above integral can be approximated to a simple Gaussian function with Doppler width equivalent to a temperature of $0.91T_{i,ave}$, where $T_{i,ave} = \frac{1}{N_i}\int d^3r n_i(r) T_i(r)$ is the average temperature of the ions. Thus, the expression for the spectrum now reduces to

$$S(\nu) = \frac{3^*\lambda^2}{2\pi}\frac{\gamma_0}{\gamma_{eff}}\int_{-\infty}^{\infty} ds \frac{1}{1+\left[\frac{2(\nu-s)}{\gamma_{eff}/2\pi}\right]^2} \frac{N_i}{\sqrt{2\pi}\tilde{\sigma}_D} \exp\left[-\frac{(\mathrm{s}-\nu_0)^2}{2\tilde{\sigma}^2_{\mathrm{D}}}\right], \quad (3.9)$$

where, $\tilde{\sigma}_D = \frac{1}{\lambda}\sqrt{\frac{0.91 k_B T_{i,ave}}{m_i}} = \frac{1}{\lambda}\sqrt{\frac{k_B T_{i,eff}}{m_i}}$ is the Doppler width with equivalent temperature as $T_{i,eff} = 0.91 T_{i,ave}$. The above equation is a Voigt profile and by fitting the spectrum data to this expression, we can extract $T_{i,eff}$ and hence the $T_{i,ave}$ of the ions.

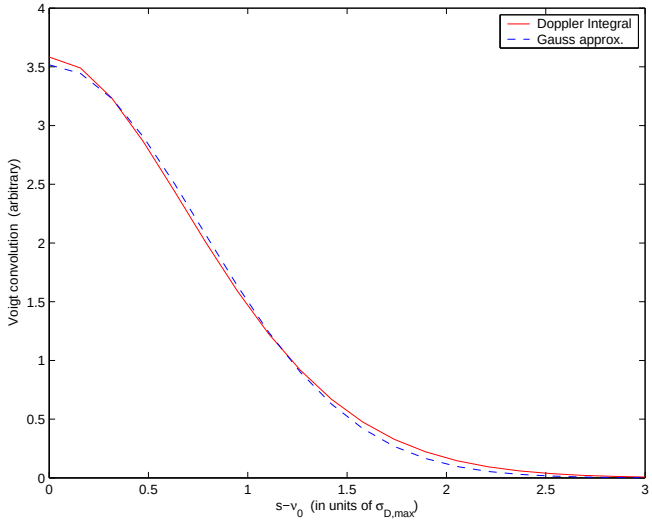


**Figure 3.2** An analytical verification showing that the weighted Doppler profile averaged over the density can be replaced by a simple Gaussian with a constant temperature, $T_{i,eff} = 0.91 T_{i,ave}$. In the figure, the continuous line is the density averaged Doppler profile, and the dashed line in the approximated Gaussian curve.

## 3.3 Determination of effective temperature considering electron screening

A procedure similar to that in the previous section is applied to consider the effects of electron screening in the plasma system. The difference here is that instead of using the simple expression of temperature given by equation 3.7, we use the local equilibrium temperature considering electronic screening given by 2.13. Electron

screening, due to shielding effects, will reduce the ion-ion interaction energy.

Using the temperature $T_i$ thus obtained from 2.13 and putting it in Eqn. 3.5, it is shown in Fig. 3.3 that in this case too the spatial integral in Eqn. 3.5 can be reduced to a simple Gaussian distribution with an effective temperature of $T_{i,eff} = 0.93T_{i,ave}$. It should be noted that the average temperature is now calculated by averaging 2.13 over the density profile.

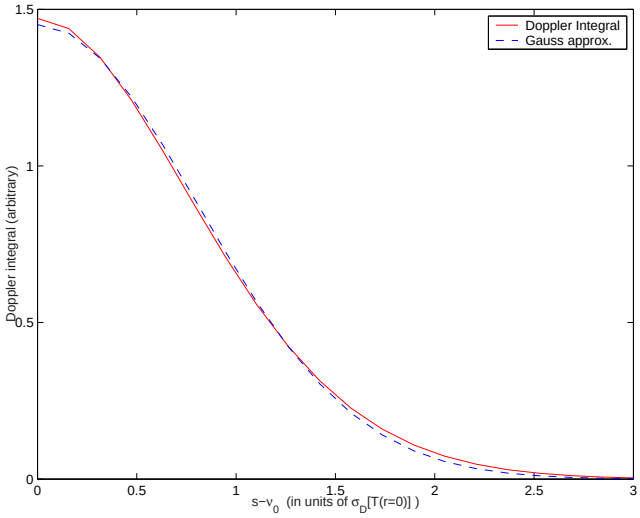


**Figure 3.3** An analytical approximation of density-averaged Doppler profile to Gaussian when screening effects of the electrons are considered. In this case, the effective temperature is $T_{i,eff} = 0.93T_{i,ave}$. The temperature is now calculated using Eqn. 2.13. The continuous line is the density average of Doppler profile, and the dashed line in the approximated Gaussian curve.

## 3.4 Calculating the efffective temperature in annular regions

As shown in the previous sections, the spatial integral in Eqn. 3.5 was approximated by a gaussian distribution from which we got an effective temperature of the ions for the plasma as a whole. The annular regions have been defined and their im-

portance already established in section 2.4. We should now investigate the effective temperature for a given annulus. The mathematical approach remains the same as described in section 3.2 and 3.3.

In the case of annular regions, the spatial integration of Eqn. 3.5 is done by considering spherical polar coordinate system. In polar coordinates, we replace $d^3r$ by $(2\pi\rho)d\rho dz$, where, the limits of $z$ is from $-\infty$ to $+\infty$. The limits of $\rho$ is $(\rho_1, \rho_2)$, where, $(\rho_1, \rho_2) = (0, 0.9),\ (0.9, 1.48),$ and $(1.48, \infty)$, in units of $\sigma$, define the three annular regions. It should also be noted that in doing the annular analysis, we use the temperature as given in Eqn. 2.13 which takes the effects of electron screening into account.

It is shown in Fig. 3.4 that the Doppler integral in each annular region can be approximated by a gaussian expression with an effective temperature, different in different annular regions. If we define the average temperature in the annuli as $T_{i,ave,reg}$, it is found that the ratio of the effective temperature ($T_{i,eff}$) to the average temperature ($T_{i,ave,reg}$) is 0.98, 0.97 and 0.92 for regions 1, 2 and 3 respectively. This ratio is called the C coefficient.

It was also shown in section 3.3 that the value of C was 0.93 for the whole volume of the plasma. Thus, without loss of much accuracy, the electron-screening effect gives the value C as $0.95 \pm 0.03$ for any of the annular regions of plasma. The plots for the gaussian approximation of the Doppler profile is shown in Fig. 3.4.

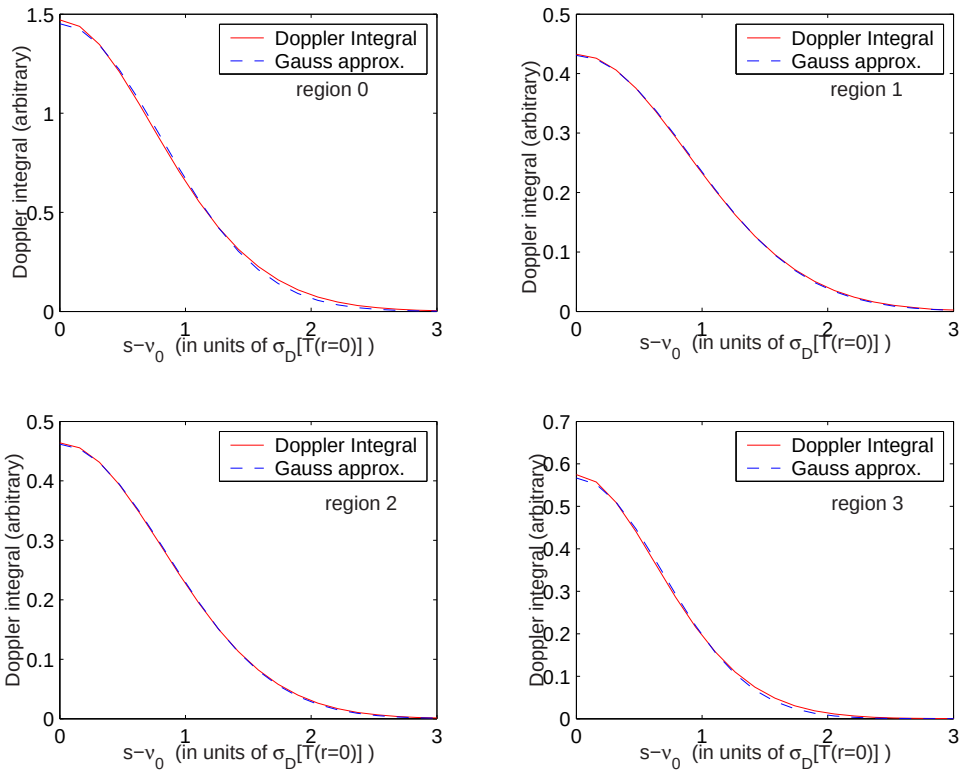


**Figure 3.4** An analytical verification showing that in the case of annular regions, the weighted Doppler profile averaged over the density can be replaced by a simple Gaussian with a constant temperature, $T_{i,eff} = CT_{i,ave,reg}$. The values of C are 0.93, 0.98, 0.97 and 0.92 for the whole plasma, region1, region2 and region3 respectively. The analysis was done by taking the electronic screening effects into consideration. In the figure, the continuous line is the density average of Doppler profile, and the dashed line in the approximated Gaussian curve.

## 3.5 Annular effective temperature considering expansion

The phenomenon of plasma expansion was briefly described in section 2.5. Here we discuss its effects on the extraction of the effective temperature in the annular regions. If $v_z$ is the average radial expansion velocity of the ions in the direction of the laser beam, then it is shown in [13] that the Doppler shift in the resonant

frequency due to the expansion velocity profile, is given by

$$\delta\nu = \frac{v_z}{\lambda} = \frac{z k_B T_e t_{delay}}{m_i \sigma_i^2 \lambda} \tag{3.10}$$

$$= \sigma_{D,ave} \frac{z}{\sigma_i} \frac{t_{delay}}{t_{exp}}, \tag{3.11}$$

where z is the distance from the center of the cloud along the direction of the laser and $t_{exp} = (\sigma_i/T_e)\sqrt{m_i T_{i,ave}/k_B}$ is the characteristic time for expansion of the cloud. In this time, the ions get enough velocity so that the Doppler width due to expansion is equal to the thermal Doppler broadening. Incorporating the above frequency in the spectrum in Eqn. 3.8, Fig. 3.5 shows that the spatial integral part can be approximated as

$$\int d^3 r n_{oi} \frac{e^{-r^2/2\sigma^2} e^{r^2/12\sigma^2}}{\sqrt{2\pi}\sigma_{D,max}} \exp\left[\frac{-\mathrm{e}^{\mathrm{r}^2/6\sigma^2}}{2\sigma^2_{\mathrm{D,max}}} (\mathrm{s} - \nu_0 - \sigma_{\mathrm{D,ave}} \frac{\mathrm{z}}{\sigma_{\mathrm{i}}} \frac{\mathrm{t_{delay}}}{\mathrm{t_{exp}}})^2\right] \tag{3.12}$$

$$\simeq \frac{N_i}{\sqrt{2\pi}\sigma_D(T_{i,eff})} \exp\left[-\frac{(\mathrm{s} - \nu_0)^2}{2\sigma^2_{\mathrm{D}}(\mathrm{T_{i,eff}})}\right], \tag{3.13}$$

where the effective Doppler profile corresponds to a temperature

$$T_{i,eff} = T_{i,ave,reg}\left[C + \left(\frac{t_{delay}}{t_{exp}}\right)^2\right]. \tag{3.14}$$

The coefficient C is the ratio of the effective temperature ($T_{i,eff}$) to the average temperature ($T_{i,ave,reg}$) when $t_{delay} = 0$, as pointed out earlier. A plot of the Doppler integral and the Gaussian approximation for various $t_{delay}$ and for different annular regions is shown in Fig. 3.5.

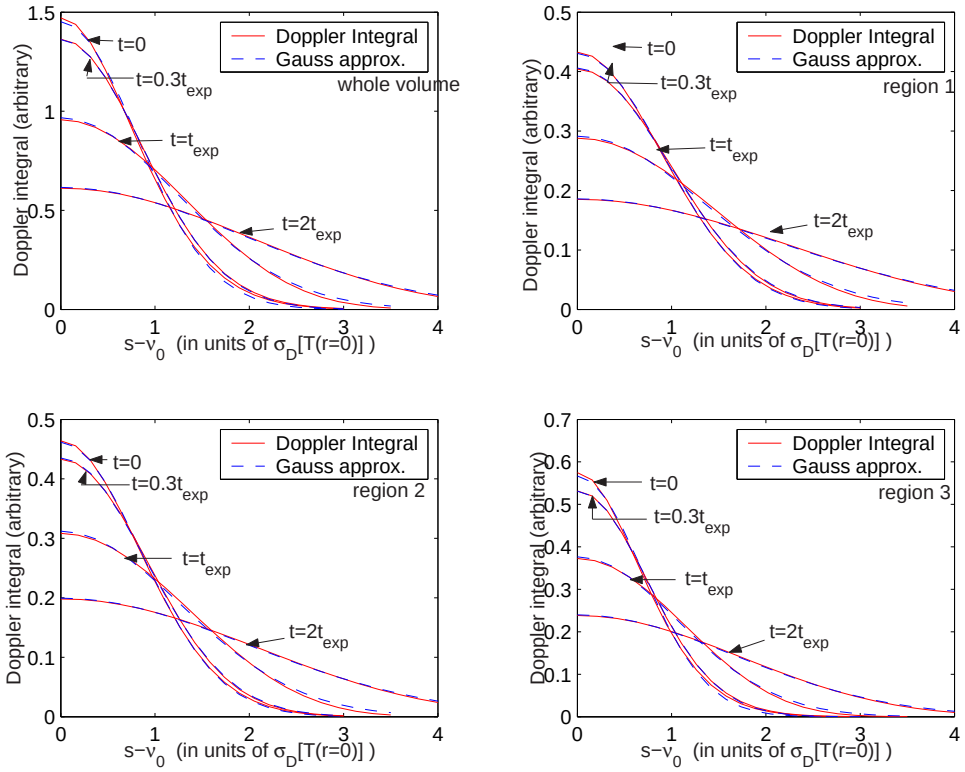


**Figure 3.5** An analytical verification showing that in the case of annular regions with the resonant frequency broadened by expansion, the weighted Doppler profile averaged over the density can be replaced by a simple Gaussian with a constant temperature, $T_{i,eff} = T_{i,ave,reg}[C + (t_{delay}/t_{exp})^2]$. Notice that as $t_{delay}$ increases, so does the Doppler width. The analysis was done by taking the electronic screening effects into consideration. In the figure, the continuous line is the density average of Doppler profile, and the dashed line in the approximated Gaussian curve.

If we include the effect of expansion on that of oscillation derived in the previous chapter, the final expression for the effective temperature in annular regions is

$$T_{eff}(t) = \int_{\rho_1}^{\rho_2} d\rho \int_{-\infty}^{\infty} dz\ (2\pi\rho)\frac{n_i(r)}{N}T_i(r)[1-cos(2\omega_{Pi}(r)t)e^{-\alpha\omega_{Pi}(r)t}]\times[C+(t_{delay}/t_{exp})^2], \tag{3.15}$$

where, we have used cylindrical coordinates with $\rho_1$ and $\rho_2$ indicating the cylindrical boundary of the annular regions and $r^2 = \rho^2 + z^2$. This is our model for $T_{eff}$.

In chapter 4 we will compare it with data and extract underlying parameters.

## 3.6 Expansion time ($t_{exp}$) is same in all the annular regions

The expansion time of our plasma is given by

$$t_{exp} = \frac{\sigma_i}{T_e}\sqrt{\frac{m_i T_{i,ave}}{k_B}}, \tag{3.16}$$

and is proportional to $\sqrt{T_{i,ave}}$. It is natural to ask whether this $T_{i,ave}$ is really the average temperature over the whole volume or the average over the corresponding annular volumes. To answer this question, $T_{i,eff}$ was extracted following the procedures described in the previous section, first, by using $t_{exp} = (\sigma_i/T_e)\sqrt{m_i T_{i,ave}/k_B}$ and then by using $t_{exp,reg} = (\sigma_i/T_e)\sqrt{m_i T_{i,ave,reg}/k_B}$. The $T_{i,eff}$ thus obtained were plotted with respect to $t_{delay}$. As shown in Fig. 3.6 it is found that only when the expansion time is given by $t_{exp} = (\sigma_i/T_e)\sqrt{m_i T_{i,ave}/k_B}$, the effective temperature follows the relation given in Eqn. 3.14. This shows that $t_{exp}$ is a global quantity, the same in all the annular regions. This fact will be very useful for all our annular analyses.

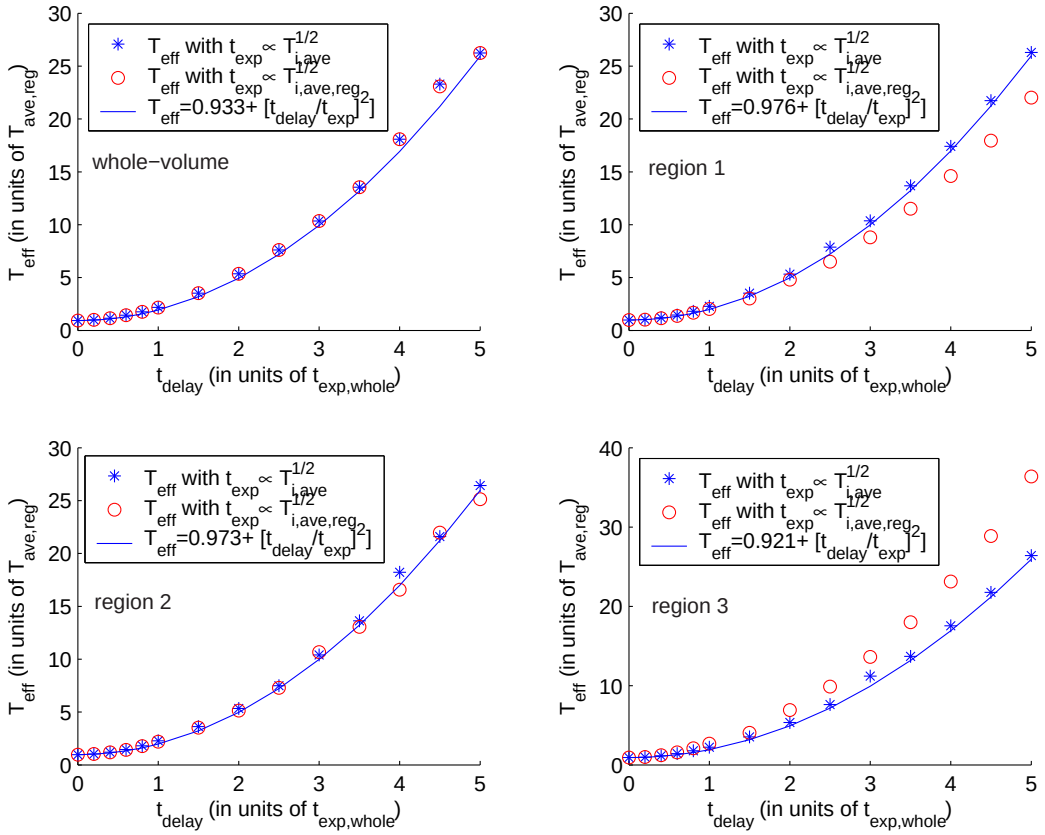


**Figure 3.6** The expansion time has to be a constant in all the regions. The expansion curve, Eqn. 3.14 doesn't fit well if $t_{exp} \propto \sqrt{T_{i,ave,reg}}$.

# Chapter 4
# Data analysis and results

After the physical background and mathematical formulations given in the previous chapters, we will show in this chapter how they fit the experimental data. The main focus of this chapter is to see the ion plasma oscillations in real data. Some trends from the fitting results will be discussed and some parameters extracted from the fittings will be compared with their values obtained from other methods.

## 4.1 Fitting the temperature data to the oscillation function

To fit the temporal variation of the ion temperature, we first extract the effective temperature, $T_{eff}$ from the data as described in section 3.4. The $T_{eff}$ is then fit to the following expression

$$T_{eff}(t) = \int_{\rho_1}^{\rho_2} 2\pi d\rho \int_{-\infty}^{+\infty} dz \frac{n_0 e^{-r^2/2\sigma_i^2}}{N} T_i(r) \left[1 - cos\{2\omega_{Pi}(r)(t-t_0)\} e^{-\alpha\omega_{Pi}(r)(t-t_0)}\right] \times \left[C + \left(\frac{t-t_0}{t_{exp}}\right)^2\right]. \quad (4.1)$$

The above equation is similar to that in Eqn. 3.15, with a few additions for the fitting to be better and slightly more flexible. The integration is now carried out in cylindrical polar coordinates (in the above equation, $r = \sqrt{\rho^2 + z^2}$). A correction term in the time, $t_0$ is incorporated in the experimental delay time, $t$. To do the fitting, we choose the following parameters- $n_0$, the peak density, $T_e$, the electron

temperature, $t_0$, the time-zero, $\beta$, a factor which made the fitted plasma size equal to $\beta\sigma_i$, and $\alpha$, the decayfactor. Out of these, $n_0$, $T_e$, $t_0$ and $\beta$ were kept constant in all the regions, because physically, these terms should be independent of the annular regions' boundary. Whereas, the decay factor $\alpha$ was allowed to vary along the regions, the variation in $\alpha$ took care of the different degree of oscillations in different regions.

The fitting was done by the method of least squares, in which the reduced $\chi^2$ defined by the formula

$$\chi^2_\nu = \frac{1}{\nu}\sum_{i=0}^{n}\left(\frac{y_{data,i} - y_{fit,i}}{e_i}\right)^2, \tag{4.2}$$

is minimized. In the above equation, $e_i$ is the experimental error assigned to each y-data values. $\nu$ is the number of the degrees of freedom and is equal to the difference between the total number of data points (n) and total number of parameters (m).

The fitting was done first for the three annular regions -1,2 and 3 and the plots of the fit and the residuals so obtained are shown in figures 4.1 and 4.2 respectively. The least square fitting was done in Matlab using the function nlinfit.m with some modifications so that it can do the reduced $\chi^2$ fitting. Using the residuals and Jacobian generated from the fits, the errors of the optimal parameters were also determined and were of the order of 10% of the parameter's value, which shows a fairly good fit. The details of the error analysis can be found in Appendix B.

In total, nine different sets of data were fit with, each having different electron temperature and peak density. These quantities were controlled by the photoionizing

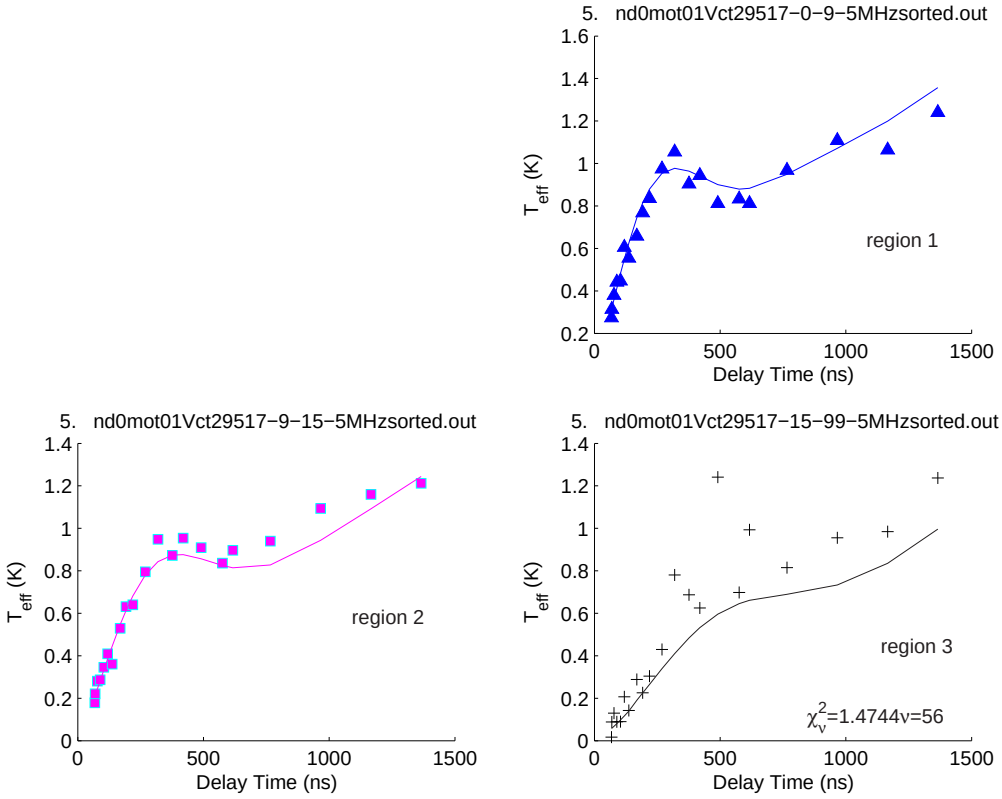


**Figure 4.1** These fits show the fits of the ion temperature of different regions to the oscillation function (Eqn. 4.1). Regions 1,2 and 3 were fitted in this case.

laser wavelength and intensity [4]. The calculated $T_e$ in the case of the data shown in Fig. 4.1 is equal to 37K. But the data also fit well in cases of high as well as low electron temperature. Two figures are shown (Fig. 4.3 and 4.4) that substantiate these claims.

Ideally, the value of $\chi^2_\nu$ should be equal to 1 for a good fit. And although we were able to fit the data to a single function in all the three regions, the value of $\chi^2_\nu$ in this kind of fitting is slightly on the high side at 1.47. With 7 parameters, $\nu$ in this case is equal to 56, and from [16] we know that in 99 out of 100 cases the value of $\chi^2_\nu$ wants

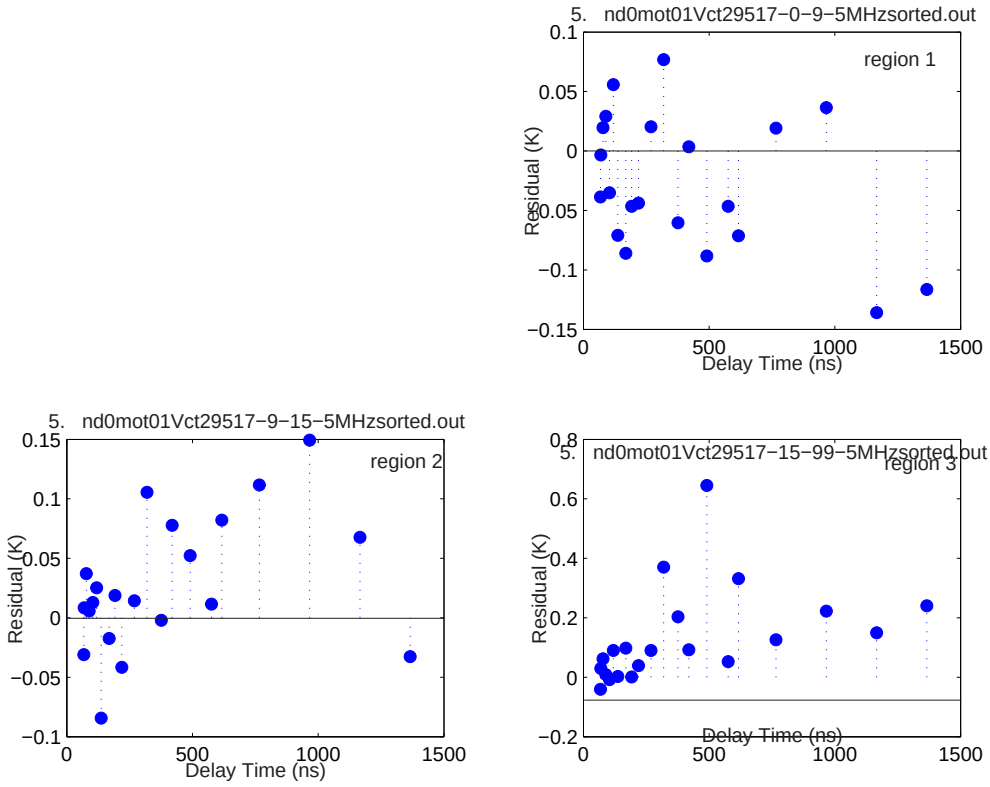


**Figure 4.2** These fits show the residuals (= data - fit) from the fit of the ion temperature of different regions. Regions 1,2 and 3 were fitted in this case.

to be less than 1.47. This corresponds to a probability of exceeding $\chi^2_\nu$ to be equal to 1%. It shows that the fit is not so good, as ideally this probability should be 50%.

This discrepancy leads us to closely examine the residuals of the plots and as can be seen from Fig. 4.2, there is a significant systematic variation in the residual for region 3 and it contributes the most to the high value of $\chi^2_\nu$. To see if our function is a bad approximation of the data, we omit the outer region in our fitting and do the analysis by fitting only regions 2 and 3. The plots and residuals so obtained are shown in figures 4.5 and 4.6 respectively. $\chi^2_\nu$ now is equal to 1.17 and this is very close

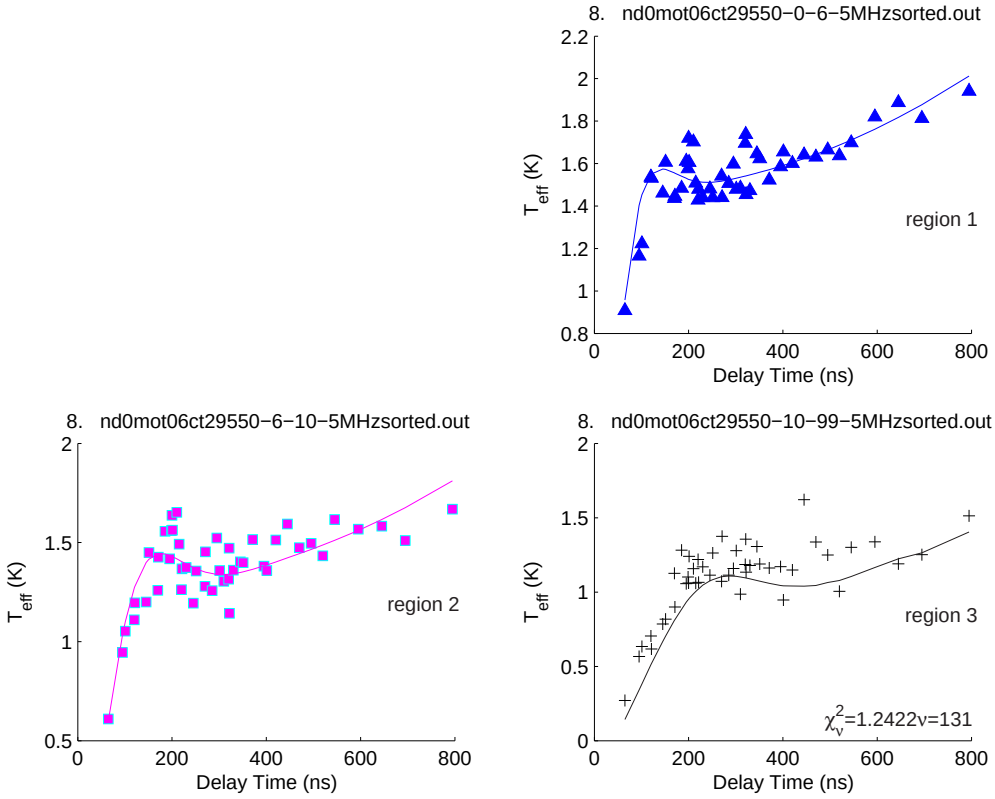


**Figure 4.3** Fits of ion temperature data for low $T_e$. These plots show the fits of the ion temperature of different regions to the oscillation function (Eqn. 4.1) when the electron temperature is comparatively low, $T_e = 11K$. Regions 1,2 and 3 were fitted in this case.

to unity. The probability of exceeding $\chi^2_\nu$ is also now about 25%. This value of $\chi^2_\nu$ is more reasonable and it suggests that our fitting-function is a good representation of our experimental data in regions 1 and 2 but does not very well fit region 3. One reason might be that the outer region is not perfectly neutral because the high energy electrons might have escaped from this region or perhaps the experimental errors assigned to the temperature (y-values) might be on the lower side as well.

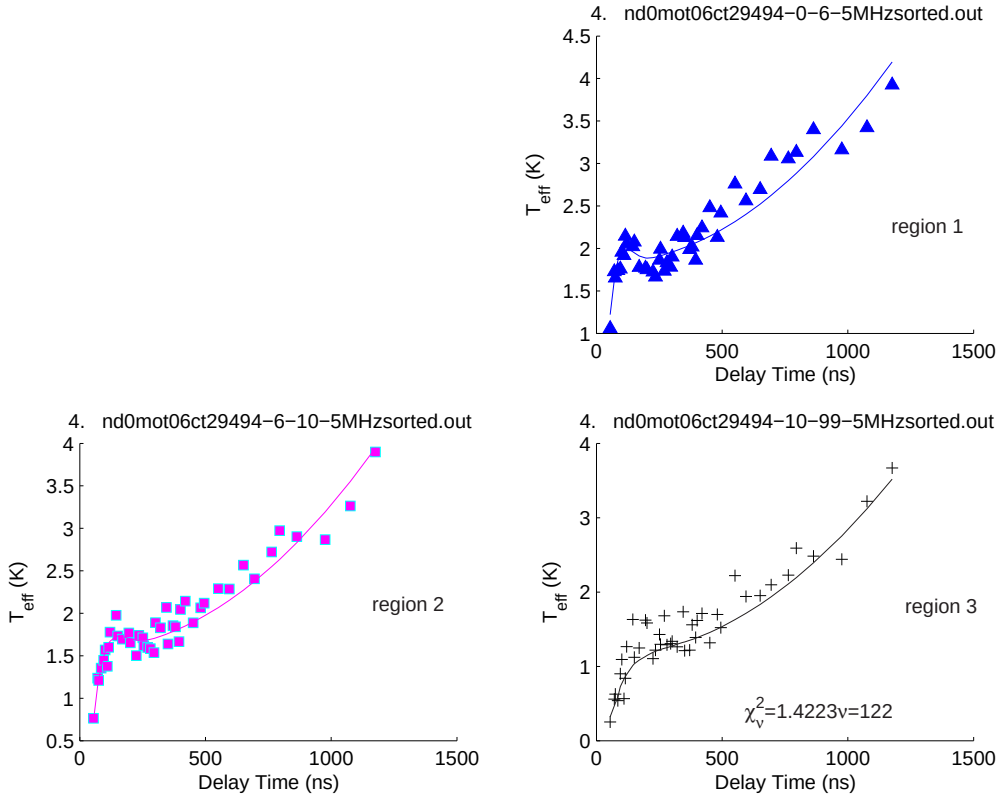


**Figure 4.4** Fits of ion temperature data for high $T_e$. These plots show the fits of the ion temperature of different regions to the oscillation function (Eqn. 4.1) when the electron temperature is comparatively high, $T_e = 56K$. Notice the short expansion time in the curves. Regions 1,2 and 3 were fitted in this case.

## 4.2 Some trends from the fits

Some of the physical quantities obtained from the fitting, viz., $n_0$, $T_e$ and $\sigma_i$ can be compared to their calculated values from other techniques. This comparison will give us more information on the reliability of our fits and the model used. The other techniques used to calculate those parameters are described here briefly. For example, the electron temperature can be calculated using the formula

$$k_B T_e = h\nu_{laser} - \Phi_{IP}, \tag{4.3}$$

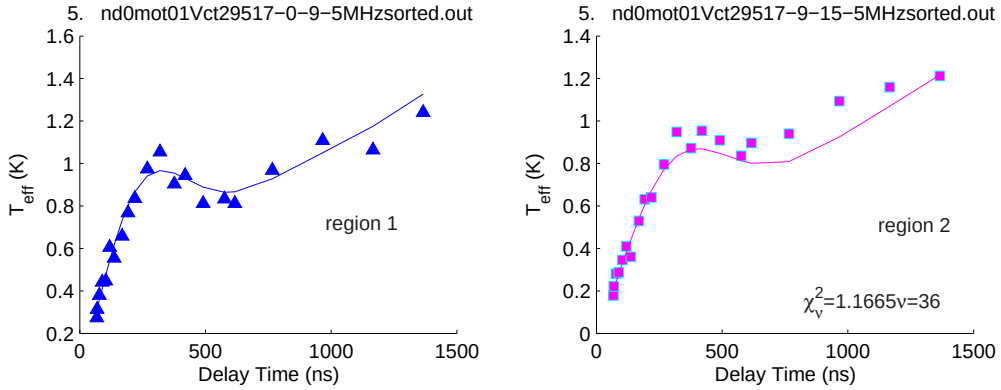


**Figure 4.5** These fits show the fits of the ion temperature of different regions to the oscillation function (Eqn. 4.1) when only region 1 and region 2 are fitted. The $\chi^2_\nu$ is very close to unity and it indicates that the fitting-function is actually a good representation of our experimental data. Regions 1 and 2 were fitted in this case.

where, $\nu_{laser}$ is the frequency of the photoionizing laser, and $\Phi_{IP} = 4.819 \times 10^{-19}$ $J$ is the ionization potential of the $^1P_1$ level of strontium. The size and peak density of the plasma were taken directly from the image.

The quantities $n_0$, $T_e$ and $\sigma_i$ were compared to their values obtained from the oscillation fitting. The plots are shown in figures 4.7, 4.8 and 4.9. As can be seen from Fig. 4.7, the values of fitted $T_e$ are generally higher than the calculated ones. This actually does not indicate an error in our analysis. It is well known that electrons heat above Eqn. 4.3 due to three-body recombination [12], disorder-induced heating [17] and continuum lowering [18]. Our analysis gives a good method to study this heating, which will be the subject of future study.

Similar plots of the fitted and calculated $n_0$ (Fig. 4.8) and the fitted and calculated ionic cloud size (Fig. 4.9) are given. They agree reasonably well.

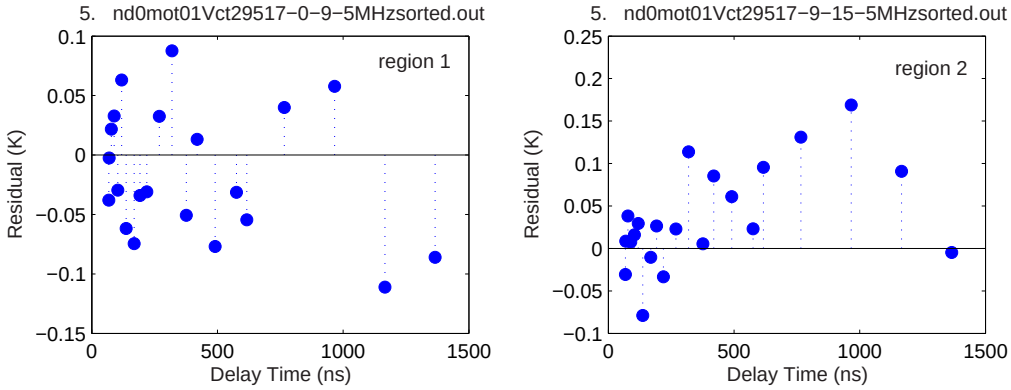


**Figure 4.6** These fits show the residuals (= data - fit) from the fit of the ion temperature of different regions. Regions 1 and 2 were fitted in this case.

### 4.2.1 Effect of damping on the oscillation data

In our model, we also account for the decay of the oscillation. This decay in oscillation is present in the system because of any damping phenomenon like ion-ion or ion-electron collisions. The effect of damping is seen clearly in Fig. 4.10. The dashed curve in the figure is a plot when there is no damping ($\alpha = 0$). The continuous curve takes the effect of damping($\alpha = 0.91$ for region 1 and $\alpha = 0.82$ for region 2) into account. Clearly, damping is an inherent feature of the oscillations that we observe. This type of decay is also shown numerically in [19] using a hybrid molecular dynamics approach. A plot of the decay factor, $\alpha$ versus the calculated $n_0$ is shown in Fig. 4.11 where it can be seen that $\alpha$ has values around unity in regions 1 and 2. The value of $\alpha$ in region 3 is not equal to 1 but as pointed out earlier, the fits in this region are not so reliable. The value of $\alpha$ is also predicted to be 1 in the simulations of [19]. This is a good agreement between theory and experiment, but

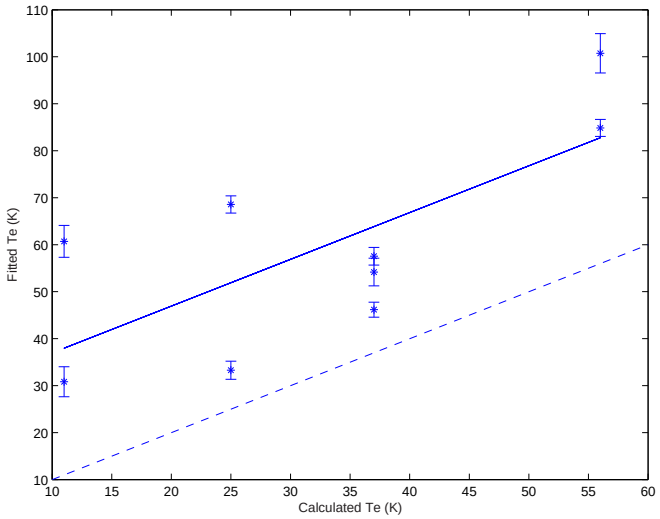


**Figure 4.7** Comparing calculated and fitted $T_e$. The y-axis has the fitted value and the x-axis has the calculated value. An x=y (dashed) line is drawn for easier comparison. The solid line is a straight line fit for the data points. Notice that the values of fitted $T_e$ are generally higher than the calculated ones.

more experiments are required to fully explore the damping.

## 4.3 Future Directions

We see that the annular analysis of kinetic energy oscillation is a powerful tool. By perfecting the plasma oscillation analysis, we can probe the dynamics of the plasma in its early stages of formation. We have described the basic analytical techniques and, will use them to study three body recombination and disorder-induced heating.

After observing temporal oscillations, we can increase our spatial resolution to observe spatial oscillations too. It has been suggested by Pohl and Pattard in [19] that the radially decreasing density causes the ions to oscillate locally. Utilizing this, they also did a theoretical simulation to show the spatial oscillations. After observing

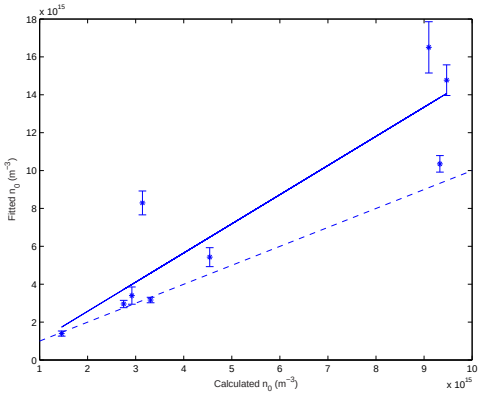


**Figure 4.8** Comparing calculated and fitted peak density $n_0$. The y-axis has the fitted value and the x-axis has the calculated value. An x=y (dashed) line is drawn for easier comparison. The solid line is a straight line fit for the data points.

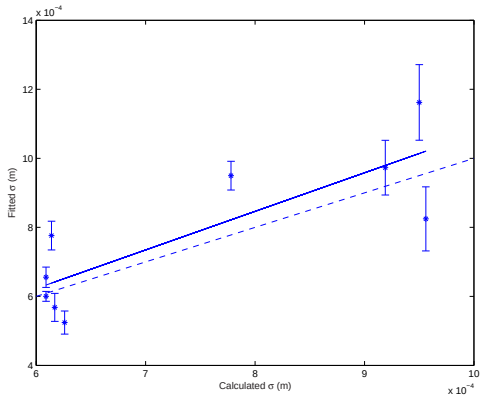


**Figure 4.9** Comparing calculated and fitted ion cloud, $\sigma_i$. The y-axis has the fitted value and the x-axis has the calculated value. An x=y (dashed) line is drawn for easier comparison. The solid line is a straight line fit for the data points.

plasma oscillations, we now understand the temporal behavior of the ions better and this information will be essential when we trap ions in future experiments.

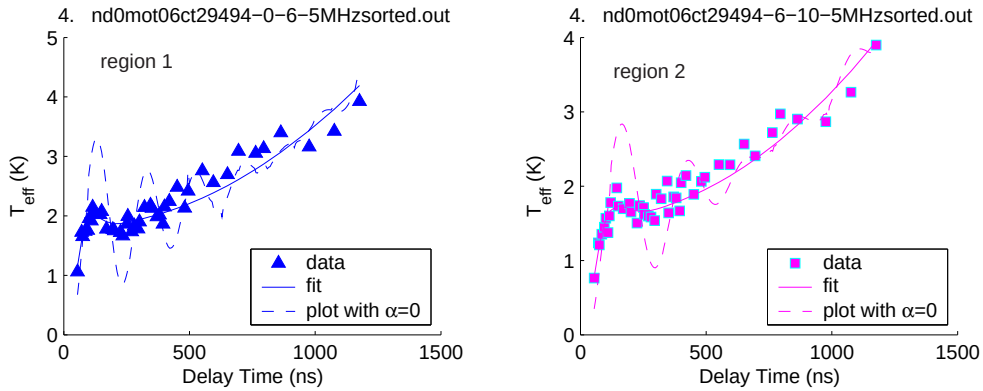


**Figure 4.10** Effect of damping on oscillations. The dashed curve is a plot when there is no damping ($\alpha = 0$) present. The continuous curve takes the effect of damping($\alpha = 1.35$ for region 1 and $\alpha = 1.38$ for region 2) into account. Clearly, damping is an inherent feature of the oscillations that we observe. In our fitting model we take the effect of damping into account.

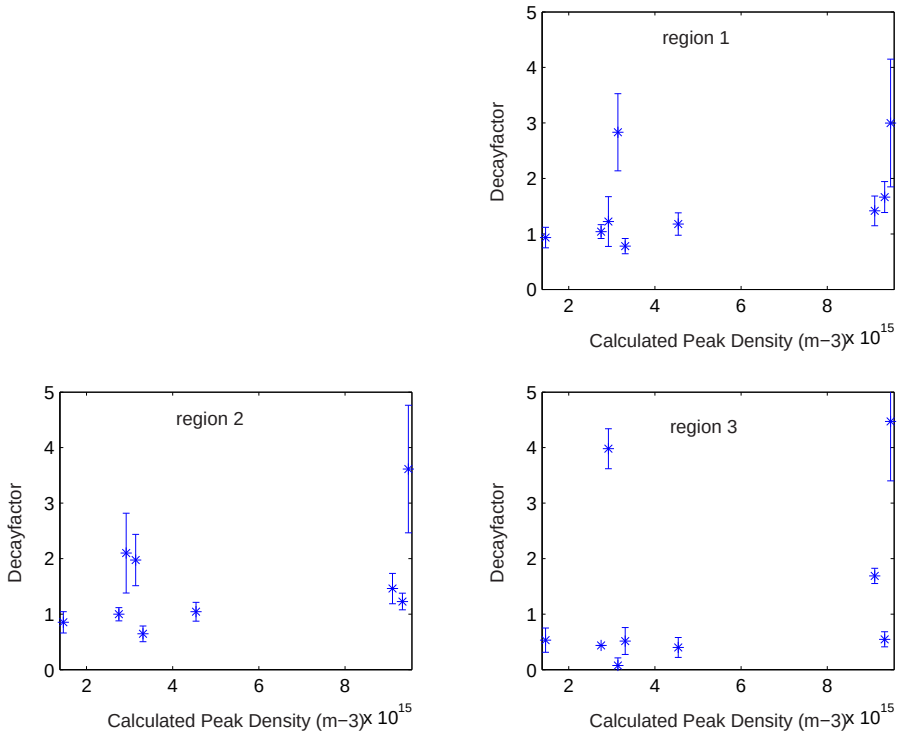


**Figure 4.11** Plots of decay factor, $\alpha$. The y-axis is the decay factor and the x-axis is the calculated peak density. In our fits, the decay factor, $\alpha$ has values around unity as shown by the simulations [19].

# Appendix A
# Code to calculate $T_i$ using equation 2.13

*The following is the Matlab code for TionofrTevector.m*

```
function TionofrTevector=myfunction(peakdens,rhovector,z,Telec,sigi)
% peak density (peakdens) in m.^-3, Te in K
% this program accepts a vector rhovector (which is useful when dblquad.m calls it
% a scalar z, and returns a vector TionofrTevector of the same size as rhovector
% rhovector and z should be in units of sigi
% This program also calls another function uex.m
for i=1:length(rhovector)
    rho=rhovector(i);
    sigi=1; % sigi=1, if rho and z are in units of sigi
    ec=1.6e-19; epson=8.85e-12;
    kb=1.38e-23; precision=1e-5;
    n=peakdens.*exp(-(rho^2+z^2)/2/sigi^2);
    Te=Telec;
    a=(3/(4*pi*n))^(1/3);
    lambda=(epson*kb*Te/(n*ec^2))^(0.5);
    k=a/lambda;
```

```
    T0=2/3*(ec^2/(4*pi*epson*a*kb))*0.5;
    Gamma0=ec^2/(4*pi*epson*kb*T0*a);
    T1=2/3*(ec^2/(4*pi*epson*a*kb))*abs(uex(k,Gamma0)+k/2); % Initial guess
    delta=abs((T1-T0)/T0);
    count=1;
    while((delta>precision)&(count<200))  % recursive approaching the solution
        Gamma1=ec^2/(4*pi*epson*kb*T1*a);
        sma=abs(uex(k,Gamma1)+k/2);
        T2=2/3*(ec^2/(4*pi*epson*a*kb))*sma;
        delta=abs((T2-T1)/T1);
        count=count+1;
        T1=T2;
    end
    TionofrTevector(i)=T1;
end
```

*The following is the Matlab code for uex.m*

```
% Based on J. Chem Phys 101,9885(1994) (Ref A),
% J. Chem Phys 105,7641(1996) (Ref B) and  PRE 56, 4671(1997) (Ref C)
function uex=myfunction(kapa,gamma);
k=kapa; g=gamma; s=1/3; kb=1.38e-23; % constants
```

```
if (g>1)
    if (k<=1)  % Ref B formula 11-16
        da=-0.003366+0.00066*k^2-0.000089*k^4;
        Ebcc=-0.895929-0.103731*k^2+0.003084*k^4-0.000131*k^6;
        a=Ebcc+da;
        b=0.565004-0.026134*k^2-0.002689*k^4;
        c=-0.206893-0.086384*k^2+0.018278*k^4;
        d=-0.031402+0.042429*k^2-0.008037*k^4;
    end
    if(k>1) % Ref C Table VIII, and polynomial fitting
        a=-0.0007*k^4+0.0154*k^3-0.1305*k^2+0.0228*k-0.9065;
        b=-0.0046*k^4+0.0538*k^3-0.2265*k^2+0.2812*k+0.4314;
        c=0.0044*k^4-0.045*k^3+0.2126*k^2-0.5031*k+0.0565;
        d=-0.0011*k^4+0.0057*k^3-0.0209*k^2+0.1406*k-0.1202;
        % this function form is only good for k<3.6
    end
    uex=(a*g+b*g^s+c+d*g^(-s))/g;
elseif ((g<=1)&(g>0)) %Ref A, Table IV and Ref C, Table VI
    gmatrix=[0 0.1 0.2 0.4 0.6 0.8 1];
    kmatrix=[0 0.2 0.4 0.6 0.8 1 1.2 1.4 2 2.6 3 3.6 4 4.6 5];
```

```
    umatrix=[0 -0.2652 -0.3483 -0.4431 -0.4962 -0.5406 -0.5717
            -0.1 -0.2809 -0.36 -0.4509 -0.5088 -0.5476 -0.5787
            -0.2 -0.3294 -0.394 -0.4794 -0.5319 -0.5708 -0.5991
            -0.3 -0.392 -0.452 -0.5251 -0.5732 -0.6087 -0.6317
            -0.4 -0.475 -0.5195 -0.5799 -0.6238 -0.6561 -0.6788
            -0.5 -0.5578 -0.5964 -0.6481 -0.6846 -0.7139 -0.7342
            -0.6 -0.648425 -0.680595 -0.724539 -0.757346 -0.782004 -0.797097
            -0.7 -0.740415 -0.770037 -0.806296 -0.831754 -0.852470 -0.869746
            -1 -1.025685 -1.042716 -1.06775 -1.085879 -1.099115 -1.110066
            -1.3 -1.319127 -1.331495 -1.348344 -1.360226 -1.369705 -1.377115
            -1.5 -1.517696 -1.527809 -1.540813 -1.549763 -1.558136 -1.563017
            -1.8 -1.815104 -1.821103 -1.831725 -1.83661 -1.843731 -1.847809
            -2 -2.009731 -2.01827 -2.027327 -2.033013 -2.037149 -2.040283
            -2.3 -2.30972 -2.315081 -2.321292 -2.327181 -2.329887 -2.332756
            -2.5 -2.50901 -2.512796 -2.520736 -2.523305 -2.525945 -2.528765];
        uex=interp2(gmatrix,kmatrix,umatrix,g,k,'spline');
    % It is good only for k<5.
else %g==0
    uex=-k/2;
end
```

# Appendix B
# Weighted $\chi^2$ fitting and parametric error determination in Matlab

In Matlab, nonlinear fitting is done by invoking the statement $[\beta, \mathrm{r}, \mathrm{J}] = \mathrm{nlinfit}(\mathrm{X}, \mathrm{y}, \mathrm{f}, \beta_0)$, where, $\beta$ is a vector containing the 'best-coefficients' and $\mathrm{r_i} = \mathrm{y_i} - \mathrm{f}(\mathrm{x_i}, \beta)$ is the residual. If the x data points are given by $(\mathrm{x_1}, \mathrm{x_2}, \ldots, \mathrm{x_n})$, then the Jacobian J is given by

$$\mathrm{J} = \overbrace{\begin{bmatrix} \frac{\partial f(x_1,\beta)}{\partial \beta_1} & \frac{\partial f(x_1,\beta)}{\partial \beta_2} & \cdots & \frac{\partial f(x_1,\beta)}{\partial \beta_k} \\ \frac{\partial f(x_2,\beta)}{\partial \beta_1} & \frac{\partial f(x_2,\beta)}{\partial \beta_2} & \cdots & \frac{\partial f(x_2,\beta)}{\partial \beta_k} \\ \vdots & \vdots & & \vdots \\ \frac{\partial f(x_n,\beta)}{\partial \beta_1} & \frac{\partial f(x_n,\beta)}{\partial \beta_2} & \cdots & \frac{\partial f(x_n,\beta)}{\partial \beta_k} \end{bmatrix}}^{\text{no. of parameters}} \tag{B.1}$$

The above method for fitting does not incorporate the weights in the $\chi^2$ minimization as it finds the best value of the parameter by minimizing $\chi^2 = \Sigma\left[\mathrm{y_i} - \mathrm{f}(\mathrm{x_i}, \beta)\right]^2$. Although nlinfit explicitly cannot do a weighted nonlinear fitting, the weighted fitting problem can be modeled to look like a non-weighted one. All we have to do is divide the $y_i$ and $f(x_i, \beta)$ values by the corresponding experimental errors in $y_i$. If $\sigma = (\sigma_1, \sigma_2, \ldots, \sigma_\mathrm{n})$ are the errors in y values, then the command $[\beta, \mathrm{r}', \mathrm{J}'] = \mathrm{nlinfitweight}(\mathrm{X}, \mathrm{y}, \mathrm{f}, \beta_0, \sigma)$ will give the best coefficients $\beta$ by minimizing $\chi^2_\mathrm{w} = \Sigma\left[\frac{\mathrm{y_i} - \mathrm{f}(\mathrm{x_i},\beta)}{\sigma_\mathrm{i}}\right]^2$. A **note of caution** must be added here: $r'$ and $J'$ are no longer the residuals and

the Jacobian respectively. In fact, $r'_i = \frac{y_i - f(x_i,\beta)}{\sigma_i}$ and

$$\mathrm{J}' = \overbrace{\begin{bmatrix} \frac{\partial f(x_1,\beta)}{\partial \beta_1}/\sigma_1 & \frac{\partial f(x_1,\beta)}{\partial \beta_2}/\sigma_1 & \cdots & \frac{\partial f(x_1,\beta)}{\partial \beta_k}/\sigma_1 \\ \frac{\partial f(x_2,\beta)}{\partial \beta_1}/\sigma_2 & \frac{\partial f(x_2,\beta)}{\partial \beta_2}/\sigma_2 & \cdots & \frac{\partial f(x_2,\beta)}{\partial \beta_k}/\sigma_2 \\ \vdots & \vdots & & \vdots \\ \frac{\partial f(x_n,\beta)}{\partial \beta_1}/\sigma_n & \frac{\partial f(x_n,\beta)}{\partial \beta_2}/\sigma_n & \cdots & \frac{\partial f(x_n,\beta)}{\partial \beta_k}/\sigma_n \end{bmatrix}}^{\text{no. of parameters}} \tag{B.2}$$

If nlinfitweight has been used, $r'$ and $J'$ have to be passed to nlparci to obtain the confidence interval of $\beta$. The statement, ci = nlparci($\beta$, r′, J′) will compute the 95% confidence interval of the parameter $\beta$. If $\delta = ci_{max} - ci_{min}$ be the width of the confidence interval, then 1-$\sigma$ error in $\beta$ can be calculated using the following formula :-

$$\Delta\beta = \frac{\delta}{2\mathrm{tinv}(0.975, \nu)} \tag{B.3}$$

Where, $\nu$ = n − k is the degree of freedom and tinv(P,$\nu$) is a function built into Matlab.

# Appendix C
# Description of the charged particle detection system in our lab

## C.1 Charged particle specifications

A charged particle detection system was constructed in our lab to initially probe the dynamics of the plasma. Its main components were a micro channel plate (MCP) from Hamamatsu Photonics and a stainless-steel Faraday Cup (FC) made in the Rice University machine shop. The FC was used as a detector or as an electrode pushing the particles to the MCP. A grid of circular wire mesh and a stainless-steel tube were also placed in front of the MCP to better guide the charged particles to the MCP. Apart from these, two copper circular discs which were divided into four quadrants each were positioned across the center of the vacuum chamber, but inside it. These served dual purposes- one, they were used to create an electric field at the center to guide the electrons or ions to the detector (MCP or FC) and second, they also reduced the stray electric field at the center which should increase the lifetime of the plasma. The longer lifetime is needed to observe the expansion of the plasma. A schematic of the charge-particle detection system is shown in Fig. C.1.

This detection is capable to detect either electrons or ions. Although the time of flight is longer for ions, their trajectory is less prone to stray electric fields inside the chamber. Another advantage in detecting ions is that when we detect electrons

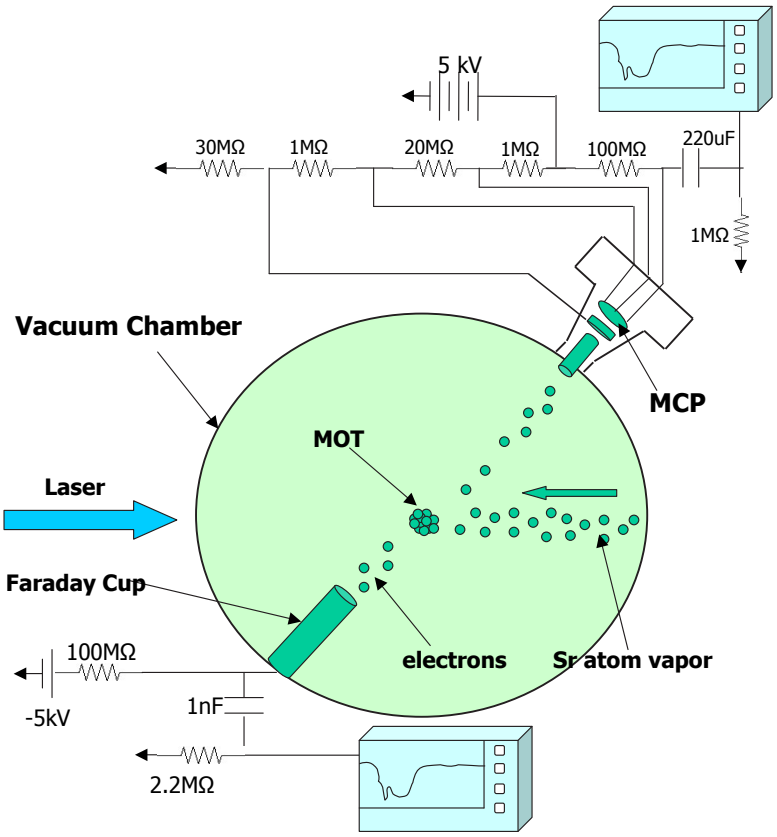


**Figure C.1** Schematic of the charge-particle detection setup

.

on the MCP, the secondary electrons generated at the FC are also detected, this phenomenon does not happen in the case of ion-detection.

## C.2 Simulating the electron trajectory using Simion 3D

The vacuum chamber and all the electrodes inside it were modeled using the ion and electron optics simulator, Simion 3D. The coding was done using geometry files which allowed us to generate the complex model of the vacuum chamber and the electrodes within. A simulation was run in Simion to find out the voltages in the

electrodes so that the charged particles are properly focused onto the MCP. A cross-sectional view of the model of the vacuum chamber generated by Simion is shown in Fig. C.2

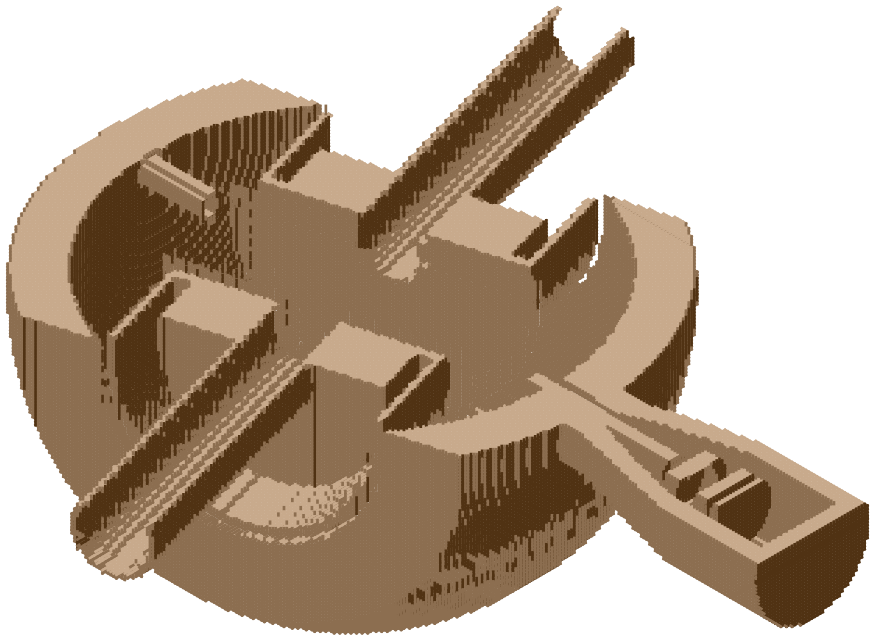

**Figure C.2** Simulation of the vacuum chamber using Simion. The vacuum chamber and all the electrodes inside it were modeled using the ion and electron optics simulator, Simion 3D.

# References

1. T. C. Killian, S. Kulin, S. D. Bergeson, L. A. Orozco, C. Orzel, and S. L. Rolston. Creation of an ultracold neutral plasma. *Phys. Rev. Lett.*, 83(23):4776, 1999.

2. H. J. Metcalf and P. van der Straten. *Laser Cooling and Trapping.* Springer-Verlag New York, New York, 1999.

3. C. E. Simien, Y. C. Chen, P. Gupta, S. Laha, Y. N. Martinez, P. G. Mickelson, S. B. Nagel, and T. C. Killian. Using absorption imaging to study ion dynamics in an ultracold neutral plasma. *Phys. Rev. Lett.*, 92(14):143001, 2004.

4. Priya Gupta. Pulsed dye laser for excitation of strontium. Master's thesis, Rice University, 2004.

5. Clayton Earl Simien. 422 nm laser. Master's thesis, Rice University, 2004.

6. L. Tonks and I. Langmuir. Oscillations in ionized gases. *Phys. Rev.*, 33(2):195, 1929.

7. W. D. Jones, H. J. Doucet, and J. M. Buzzi. *An introduction to the linear theories and methods of electrostatic waves in plasmas.* Plenum Press, New York, 1985.

8. T. B. Mitchell, J. J. Bollinger, X. -P. Huang, W. M. Itano, and D. H. E. Dubin.

Direct observations of the structural phases of crystallized ion plasmas. *Phys. Plasmas*, 6(5):1751, 1999.

9. M. S. Murillo. Using fermi statistics to create strongly coupled ion plasmas in atom traps. *Phys. Rev. Lett.*, 87(11):115003, 2001.

10. S. Hamaguchi, R. T. Farouki, and D. H. E. Dubin. Triple point of yukawa systems. *Phys. Rev. E*, 56(4):4671, 1997.

11. S. Kulin, T. C. Killian, S. D. Bergeson, and S. L. Rolston. Plasma oscillations and expansion of an ultracold neutral plasma. *Phys. Rev. Lett.*, 85(2):318, 2000.

12. F. Robicheaux and J. D. Hanson. Simulated expansion of an ultra-cold, neutral plasma. *Phys. Plasmas*, 10(6):2217, 2003.

13. T. C. Killian, Y. C. Chen, P. Gupta, S. Laha, Y. N. Martinez, P. G. Mickelson, S. B. Nagel, A. D. Saenz, and C. E. Simien. Absorption imaging and spectroscopy of ultracold neutral plasma. *J. Phys. B*, 38:351, 2005.

14. A. E. Siegman. *Lasers*. University Science Books, Sausolito, California, 1986.

15. T. Pohl, T. Pattard, and J. M. Rost, Private communication (2004).

16. Philip R. Bevington and D. Keith Robinson. *Data reduction and error analysis for the Physical Sciences*. McGraw-Hill, Inc., 1992.

17. S. G. Kuzmin and T. M. O'Neil. Numerical simulation of ultracold plasmas. *Phys. Plasmas*, 9(9):3743, 2002.

18. S. Mazevet, L. A. Collins, and J. D. Kress. Evolution of ultracold neutral plasmas. *Phys. Rev. Lett.*, 88(5):55001, 2002.

19. T. Pohl, T. Pattard. Strong coupling effects in the relaxation dynamics of ultracold neutral plasmas. Submitted, arXiv/physics/0503018.